Motion Estimation in Static Magnetic Resonance Elastography

By

Elena Popel

Submitted to the graduate degree program in Electrical Engineering and the Graduate Faculty of the University of Kansas in partial fulfillment of the requirements for the degree of Doctor of Philosophy.

_____
Glenn Prescott (Co-Chair)

_____
Mehmet Bilgen (Co-Chair)

Committee members: _____
Arvin Agah

_____
Brian Potetz

_____
Irina V. Smirnova

Date defended: _____

The Dissertation Committee for Elena Popel certifies that this is the approved version of the following dissertation

Motion Estimation in Static Magnetic Resonance Elastography

_____
Glenn Prescott (Co-Chair)

_____
Mehmet Bilgen (Co-Chair)

Committee members: _____
Arvin Agah

_____
Brian Potetz

_____
Irina V. Smirnova

Date approved: _____

To my Boys

Abstract

Elastography is the imaging of the biomechanical properties of a tissue to detect and diagnose abnormal pathologies in a variety of disease conditions. Static Magnetic Resonance Elastography (MRE) is a modality of elastography that uses Magnetic Resonance Imaging (MRI) principles for data acquisition from a biological sample under external loading. An estimation of the mechanical deformation of the loaded sample from its Magnetic Resonance (MR) images constitutes a key component of the static MRE. Efforts in this area of research have mainly been focused on developing data acquisition protocols and motion estimation algorithms for producing high quality elastography images. So far, however, progress made in static MRE remains limited in both clinical and experimental fields.

This dissertation work performed a comprehensive investigation of the data acquisition, pre-processing, and motion analysis stages of the static MRE modality. First, a mechanical device was introduced to reliably apply repetitive external compression to the sample. The design of this device and how it was interfaced with the scanner for gated data acquisition are described in detail. Next, MRI basics are summarized, and the use of tagged MRI sequence as the data acquisition protocol is justified. Optimal parameters that led to the best quality tagged MRI data were determined by taking the repetitiveness of the compression and the use of tag lines into consideration. Lastly, two reliable motion estimation algorithms were implemented and successfully tested on a variety of synthetic and real MRE data. After adjusting the parameters of the techniques using the prior knowledge of the

features of the tagged MR images, both Iterative and One-step Optical Flow (OF) algorithms consistently produced acceptable results. It was found, that while applied to the real data, the Iterative OF algorithm slightly outperforms the One-step OF algorithm. The results of the testing are provided and discussed.

This research is interdisciplinary and embraces concepts from the fields of Physics, Image Processing, Computer Vision, Algorithmics, Electrical Engineering, and Biomedical sciences. Future extensions of the research include a variety of studies on phantoms with an inclusion, small oncology animal models, and possibly followed by clinical human research that would contribute to improving the reliability, accuracy, and speed of tumor detection. Other possible applications may involve processing of different types of MRI data, such as cardiac tagged gated MRI.

Acknowledgements

I would like to thank Dr. Mehmet Bilgen and Dr. Glenn Prescott for their constant support and advice while performing this research. I am also thankful to my former co-advisers Dr. John Gauch and Dr. Costas Tsatsoulis for all of their useful contributions and suggestions.

Email conversations with Dr. John Barron from the Department of Computer Science, The University of Western Ontario, London, Ontario, Canada, helped me understand issues of Optical Flow algorithms and their limitations. I wish to thank my former committee members Dr. Donna Haverkamp, Dr. Mikhail Medvedev, and Dr. Arcady Mushegian, as well as my current committee members Dr. Irina Smirnova, Dr. Brian Potetz, and Dr. Arvin Agah for reading the drafts of my dissertation and giving useful remarks at different stages of my work.

I am also grateful to my PhD classmates Ms. Eera Mittur, Dr. Svetlana Arshavski, Dr. Tareq Alrefae, and Dr. Mohammed D. Alenezy for their great help and support and to the teaching and administrating staff of the EECS Department at the University of Kansas for their contributions during the years of my studies at the department.

On a personal level, I would like to thank my friend and former husband Denis Popel for all his help, understanding, and great patience during the long years of my studies. Thank you to my dearest beloved family, two sons, Danila and Mikita, my husband Bruce, and my parents, and, of course, to all the great and close friends from all over the world who have provided a lot of love and constant support.

Elena Popel

Table of Contents

List of Figures

List of Tables

Chapter 1
Introduction

A variety of biomedical imaging modalities is currently used in practice, and new ones are also being developed for potential applications in preclinical research and clinical environments. Magnetic Resonance Elastography (MRE) is one of these modalities and constitutes the main focus of this dissertation.

In this introductory chapter, the motivation and driving problem for the research is described (Section 1.1), followed by an introduction of the research hypothesis as well as the research plan and evaluation in Sections 1.2 and 1.3, respectively.

1.1 Motivation and Driving Problem

Tissue elasticity properties carry important diagnostic information for a wide range of diseases associated with inflammation and altered soft tissue biomechanics. For example, a majority of tumors, liver fibrosis, and different muscle pathologies are intrinsically characterized by their properties of abnormal stiffness. If spatial changes in biomechanical properties or in short elasticity are to be a valuable indicator of a disease or pathology, reliable and accurate tools are needed for objectively assessing the stiffness directly by using *in vivo* measurements. MRE has recently been proposed to address this need. MRE uses Magnetic Resonance Imaging (MRI) as the principle of data gathering, and it is further divided based on the implementation of the acquisition sequence. In this research, we consider data acquisition using tagged MRI and tissue motion measurements estimated indirectly using a sequence of two or more tagged images. The sequence of tagged images that encodes the tissue motion is acquired while the compression applied by an external actuator to the biological

tissue is in progress. An important step in post-processing is to accurately quantify the motion resulting from the compression using the images.

In the literature, algorithms and image processing techniques have been described to estimate motion between two given images in a sequence. However, the majority of the existing motion estimators cannot be directly applied to process the tagged images. Special adaptation, implementation, modifications, and optimization of the existing techniques are required. It is also desirable that the estimator would perform well within reasonable error limits in the motion estimates. The goal of this project was to implement a robust algorithm to estimate the tissue motion in tagged images. Optical Flow (OF) algorithms have been successfully used as motion estimators in a wide range of applications, but these algorithms have yet to be applied to MRE. Because of their relatively well understood behavior and performance limits, in this dissertation we examined what OF can offer in post-processing of the sequential images with motion encoded inherently by the tagged lines under external compression.

1.2 Research Hypothesis

The results from our initial evaluation suggested that it is possible to use OF in analyzing tagged MRI data. Based on these results, we hypothesized that the OF algorithm could perform in MRE as well as it did in other applications provided that a suitable data acquisition mechanism was built and a new set of constraints and a priori knowledge were appropriately incorporated into the design and implementation of the algorithm. Our research aimed at testing this hypothesis. To accomplish this

task, we performed critical preliminary work and essential procedures as listed in the following.

1.3 Research and Evaluation

MRE involves discrete application of external compression and simultaneous acquisition of time-sequential MR images followed by off-line processing of acquired data to estimate the motion experienced by the tissue. To successfully generate the motion maps in MRE in this research, the following work was performed:

(i) Synthetic tagged MRI representing images of soft biological tissues with different compressibility features were generated and used as a numerical simulation medium. The process included producing sequences of images with standard patterns of tag lines, different levels of signal-independent additive noise, and different models of tissue motion. The synthetically generated data ranged from a simple translation of the simulated uniformly soft tissue to a more complicated model with a stiff 2-D cylindrical inclusion embedded into a soft background biological media.

(ii) The performances of the OF algorithms were demonstrated using the synthetic data, and their accuracies were quantified using error analysis.

(iii) An effective tissue compression device with electromagnetic components was built to operate within a 9.4 Tesla MRI scanner (Varian, Inc., Palo Alto, Ca).

(iv) Tagged MRI protocol was optimized for tag line generation and image acquisition.

(v) A set of agar-based phantoms was developed to represent biological tissue with a stiff region. These phantoms were used to acquire tagged MRI data, which were then used to evaluate the proposed algorithms.

Chapter 2
Background

Biomedical imaging is an important and one of the most rapidly advancing areas of research in medicine. Many imaging modalities already exist and are widely used in diagnostics radiology as well as in treatment assistance in oncology. MRI is one of these modalities, and it provides anatomical, structural, functional, and biochemical information about the underlying tissue. MRI is a non-invasive and non-ionizing technique. MRE uses MRI as a data acquisition method, making it non-invasive and non-ionizing, but including additional methodological steps to compress the tissue with an external source (actuator) and post-process the MRI data for estimating the resulting motion. Here, we first briefly summarize the basic principles of the image formation in MRI and then cover background material relevant to the performed research in detail. The detailed treatment of MRI can be found in [1].

In this chapter, the background information concerning the area of the research based on the literature review is provided. The chapter is organized as follows: Section 2.1 introduces the basics of MRI physics, and Section 2.2 gives some insides on the assessment of soft tissue elastic properties, followed by principles of Elastography in general and MRE in particular.

2.1 Basic Physics of MRI

The atomic nuclei possess spin angular momentum, a characteristic that allows them to interact with an external magnetic field [1, 2]. This interaction provides the basis for the MRI principles. Spin can be viewed as an angular momentum arising from rotation of the nucleus around an axis through its center. The most used nucleus

in MRI is hydrogen (^{1}H) due to its abundance in biological tissue. ^{1}H experiences two spin energy states: spin-up and spin-down. Within an external magnetic field $\vec{B}_0$, the magnetic moment $\vec{\mu}$ of a spin $\vec{S}$ can be written as

$$\vec{\mu} = \gamma \vec{S} \tag{2.1}$$

where γ is the gyromagnetic ratio and is equal to 42 MHz/T for ^{1}H.

The energy of the spin is expressed as

$$E = -\vec{\mu} \cdot \vec{B}_0 \tag{2.2}$$

and the energy transition between two states is

$$\Delta E = \hbar \omega \tag{2.3}$$

where $\hbar$ is the Plank constant, and ω is the frequency of the electromagnetic radiation. Transition between two adjacent states occurs at the Larmor frequency $\omega_0 = \gamma B_0$. For ^{1}H, ω_0 = 420 MHz at B_0=10 T. With the interaction between $\vec{\mu}$ and $\vec{B}_0$, $\vec{\mu}$ tends to align with $\vec{B}_0$. However, due to thermal fluctuations, $\vec{\mu}$ usually orients at an angle to and precesses around $\vec{B}_0$.

2.1.1 Macroscopic View

Consider an ensemble of ^{1}H nuclei in an external magnetic field $\vec{B}_0$ that is oriented in the *z* direction. The equilibrium distribution of the spins is the Boltzmann distribution in each state (spin-up or spin-down). The magnetization of the ensemble of spins is the mean of the magnetic moments:

$$\vec{M} = \langle \vec{\mu} \rangle \tag{2.4}$$

The external magnetic field is in the *z* direction. While the transverse components of each $\vec{\mu}$ are randomly oriented in the transverse (*x-y)* plane and $M_x = M_y = 0$, the longitudinal component M_z does not vanish. For ^{1}H, the magnetization can be calculated as

$$M_z = \frac{1}{2}\gamma\hbar N_0 \frac{e^{\frac{\gamma\hbar B_0}{2kT}} - e^{-\frac{\gamma\hbar B_0}{2kT}}}{e^{\frac{\gamma\hbar B_0}{2kT}} + e^{-\frac{\gamma\hbar B_0}{2kT}}} = \frac{1}{2}\gamma\hbar N_0 \cdot \tanh\left(\frac{\gamma\hbar B_0}{2kT}\right) \tag{2.5}$$

where N_0 is the total number of spins, *T* is the temperature, and k_B is the Boltzmann constant. For B_0 = 10 T at room temperature (~300 K), $M_z \sim 10^{-32} N_0 \quad J/T$. For 1 mg of water, $N_0 \sim 10^{19}$ and $M_z \sim 10^{-13}\ J/T$. M_z values can be measured by using the induction principle (Faraday's law) in MRI [3].

2.1.2 Dynamics of Magnetization

In the presence of the external field $\vec{B}_0$, the equilibrium state of the magnetization of a biological tissue sample is $M_x = M_y = 0$ and $M_z = M_{z0}$ where M_{z0} is given in Eq. 2.5. If another magnetic field is introduced to the system, the magnetization moves away from the equilibrium. After the additional magnetic field is eliminated, the magnetization relaxes back to the original equilibrium state. The relaxation process highly depends on the sample structure. In MRI, the characteristic of this relaxation is measured to obtain the information about the biological structure of the sample.

With $\vec{B}_0$ in the longitudinal direction present, the spins in a sample precess at a small angle around $\vec{B}_0$ with the Larmor frequency ω_0. Another magnetic field $\vec{B}_1$ that is perpendicular to $\vec{B}_0$ is applied to produce the excitation of the spins. Under the influence of $\vec{B}_1$, the spins tip away from $\vec{B}_0$ with a greater angle. In order to efficiently perturb the spins, $\vec{B}_1$ has to rotate with the spins. The rotational frequency of $\vec{B}_1(t)$ is the same as the Larmor frequency. Note that $\vec{B}_1$ is much weaker than $\vec{B}_0$ ($\vec{B}_1 / \vec{B}_0 \sim 0.1\%$) [4].

To describe the dynamics of the excited magnetization of a sample, it is convenient to use a rotating reference frame in which $\vec{B}_1(t)$ is constant [1]. Consider a spin that precesses around $\vec{B}_0$ in the clockwise direction (see Fig. 2.1). The transverse plane (*x'-y'*) of the rotating frame rotates with the precession in the same direction with the Larmor frequency ω_0. The transformations between the rotating frame $(\vec{e}_{x'}, \vec{e}_{y'}, \vec{e}_{z'})$ and the laboratory frame $(\vec{e}_x, \vec{e}_y, \vec{e}_z)$ is then

$$\begin{aligned} \vec{e}_{x'} &= \cos(\omega_0 t)\vec{e}_x - \sin(\omega_0 t)\vec{e}_y \\ \vec{e}_{y'} &= \sin(\omega_0 t)\vec{e}_x + \cos(\omega_0 t)\vec{e}_y \\ \vec{e}_{z'} &= \vec{e}_z \end{aligned} \qquad (2.6)$$

In the laboratory frame, $\vec{B}_1(t)$ is in the transverse plane and is rotating with the spin as

$$\vec{B}_1(t) = B_1\left[\cos(\omega_0 t)\vec{e}_x - \sin(\omega_0 t)\vec{e}_y\right] = B_1\vec{e}_{x'} \qquad (2.7)$$

In the rotating frame, therefore, $\vec{B}_1$ is a constant field in the *x* direction. Note that $\vec{B}_0$ is still in the longitudinal direction in both laboratory and rotating frames.

The dynamics of $\vec{M}$ in the presence of $\vec{B}_0$ and $\vec{B}_1(t)$ is governed by the Bloch equation

$$\frac{d\vec{M}}{dt} = \gamma \vec{M} \times \vec{B} \tag{2.8}$$

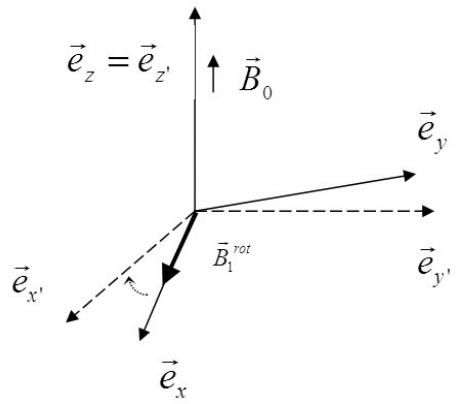

Figure 2.1: Laboratory and Rotating Frames.

In a rotating frame, the time derivative of $\vec{M}$ can be written as

$$\frac{d\vec{M}}{dt} = \frac{\partial \vec{M}}{\partial t} + \vec{\Omega} \times \vec{M} \tag{2.9}$$

where $\vec{\Omega} = -\omega_0 \vec{e}_{z'}$, $\vec{M} = M_{x'}\vec{e}_{x'} + M_{y'}\vec{e}_{y'} + M_z\vec{e}_z$ and

$$\frac{\partial \vec{M}}{\partial t} = \frac{dM_{x'}}{dt}\vec{e}_{x'} + \frac{dM_{y'}}{dt}\vec{e}_{y'} + \frac{dM_{z'}}{dt}\vec{e}_{z'} \tag{2.10}$$

Then Bloch equation becomes

$$\frac{d\vec{M}}{dt} = \gamma \vec{M} \times \left(\vec{B} + \frac{\vec{\Omega}}{\gamma} \right) \tag{2.11}$$

where $\vec{B} = B_0\vec{e}_z + B_1\vec{e}_{x'}$. With the resonance condition of $\vec{\Omega} = -\gamma\vec{B}_0$, the Bloch equation in the rotating frame reduces to

$$\frac{d\vec{M}}{dt} = \omega_1\left(\vec{M} \times \vec{e}_{x'}\right) \tag{2.12}$$

where $\omega_1 = \gamma B_1$. Consider an initial condition of a typical MRI measurement in which $M_{x'} = M_x = 0$, $M_{y'} = M_y = 0$, and $M_{z'} = M_z = M_{z0} = 0$ at $t = 0$. $\vec{M}(t)$ can be solved from Eq. 2.12 as

$$\begin{aligned} M_{x'} &= 0 \\ M_{y'} &= M_{z0}\sin(\omega_1 t) \\ M_{z'} &= M_{z0}\cos(\omega_1 t) \end{aligned} \tag{2.13}$$

where M_{z0} is the maximum (longitudinal) value of the magnetization.

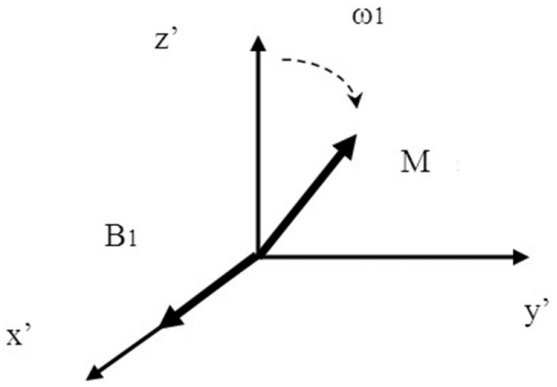

Figure 2.2: Precession of $\vec{M}$ around $\vec{B}_1$ in Rotating Frame.

As shown in Eq. 2.13, $\vec{M}$ precesses around $\vec{e}_{x'}$ with angular velocity ω_1 in the rotating frame (see Fig. 2.2). In MRI, $\vec{B}_1(t)$ is usually applied as a pulse. For a pulse $\vec{B}_1(t)$ with a duration of Δt, the angle precessed (tipped away from $\vec{e}_{z'} = \vec{e}_z$) for $\vec{M}$ is

$\theta_{\Delta t} = \omega_1 \Delta t = \gamma B_1 \Delta t$. In MRI measurement, a 90° tip is usually preferred for a strong signal. For B_1 ~10 mT, the duration of the pulse $\vec{B}_1(t)$ is about 2 ms [4].

2.1.3 Relaxation Mechanism

Consider the case of a 90° tip in which $\theta_{\Delta t} = 90^\circ$ of $\vec{M}$ due to $\vec{B}_1(t)$ [1]. Right after $\vec{B}_1(t)$ is turned off, $M_x = M_{y'} = M_{z0}$, $M_y = M_{x'} = 0$, and $M_z = M_{z'} = 0$. With the time, the restoration of $\vec{M}$ to its equilibrium ($M_z = M_{z0}, M_x = M_y = 0$) occurs via two processes. The first process is the release of the magnetic energy in the form of heat from the spins to the surrounding materials. This process is directly linked to the alignment of $\vec{M}$ to $\vec{B}_0$ as M_z recovers from 0 to M_{z0}.

The restoration of the M_z is governed by

$$M_z = M_{z0}(1 - e^{\frac{-t}{T1}}) \tag{2.14}$$

where T_1 is the longitudinal relaxation time. The second restoration process of $\vec{M}$ is the decay of M_x. After $\vec{B}_1$ is turned off, M_x is gradually decaying from $M_x = M_{z0}$ to $M_x = 0$. During this process M_x is measured by a closely placed coil. This measurement is commonly referred to as an MRI signal. The decay of the MRI signal is therefore

$$M_x = M_{z0} e^{\frac{-t}{T2}} \tag{2.15}$$

where T_2 is the transverse relaxation time. Typically, T_1 and T_2 depend on the biological tissue properties and the strength of the external magnetic field.

2.1.4 Gradient Coil, *k*-Space, and Image Formation

Consider a biological body that contains only three small distinct regions where there is hydrogen spin density (Fig. 2.3) [5]. In reality, the entire body would contribute to the formation of the MR signal. When these regions of spin experience the same external magnetic field, only one peak is produced in the spectrum (Fig. 2.3).

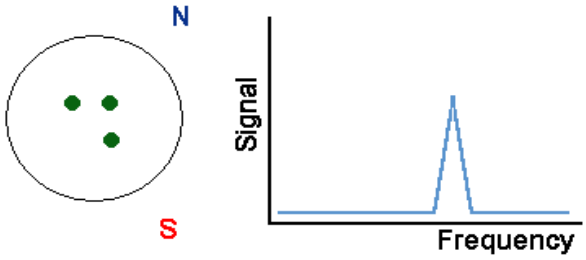

Figure 2.3: Three Distinct Regions with Hydrogen Spin Density and a Single Peak in the Spectrum Produced under the same Magnetic Field Strength.

If each of the regions would experience a unique magnetic field, then it would be possible to image their positions. A gradient in the magnetic field allows accomplishing of this localization task. A magnetic field gradient is a variation in the magnetic field with respect to a position. A one-dimensional magnetic field gradient is a variation with respect to one direction, while a two-dimensional gradient is a variation with respect to two. The most useful type of gradient in magnetic resonance imaging is a one-dimensional linear magnetic field gradient. A one-dimensional magnetic field gradient along the x axis in a magnetic field B_0, indicates that the

magnetic field is increasing in the x direction. The length of the vectors represents the magnitude of the magnetic field (Fig. 2.4). The symbols for a magnetic field gradient in x, y, and z directions are G_x, G_y, and G_z.

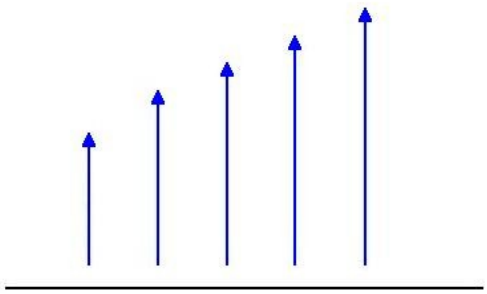

Figure 2.4: Field Gradient.

The point in the center of the magnet where $(x, y, z) = 0,0,0$ is called the isocenter of the magnet. The magnetic field at the isocenter is B_0 and the resonant frequency is ω_i (Fig. 2.5).

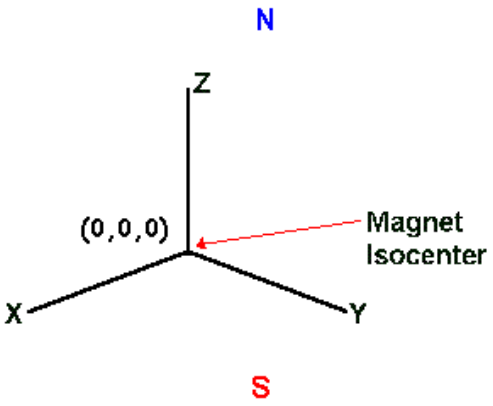

Figure 2.5: Isocenter of the Magnet.

If a linear magnetic field gradient is applied to the biological sample in Figure 2.3 with three spin containing regions, the three regions experience different magnetic fields. The result is a spectrum with more than one peak (Fig. 2.6). The amplitude of the signal is proportional to the number of spins in a plane perpendicular to the gradient. This procedure is called frequency encoding and causes the resonance frequency to be proportional to the position of the spin.

$$\omega_0 = \gamma (B_o + x G_x) = \omega_i + \gamma x G_x \qquad (2.16)$$

$$x = (\omega_0 - \omega_i) / (\gamma G_x) \qquad (2.17)$$

This principle forms the basis behind all magnetic resonance imaging [6].

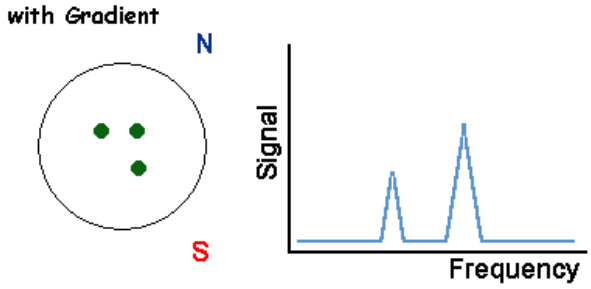

Figure 2.6: Three Distinct Regions with Hydrogen Spin Density and Two Different Peaks in the Spectrum Produced with Magnetic Field Gradient Applied along Horizontal Direction.

The basic principles of image formation can be explained by using *k*-space [5]. *k*-space is an array of numbers whose inverse Fourier Transform (*iFT*) is the MR image in the spatial domain. Each element in a *k*-space contains information about every image pixel. So, in order to have a complete image of good quality, each element in the *k*-space has to be filled with the acquired MR signal. Filling the *k*-space requires

repetitive signal acquisition, which explains why MR scans take a relatively long time. In this regard, the faster the *k*-space can be filled, the quicker the image is acquired [5].

The parameter k is given by

$$k = \gamma G t \tag{2.18}$$

where G is the amplitude of the frequency encoding gradient and t is the duration of this gradient ($G t$ is the 'area under the gradient').

An example of an image acquisition pulse sequence is given in Figure 2.7. Varying the angle of the gradient θ is accomplished by the application of linear combinations of two gradients.

To make MR imaging viable we have to have the ability to capture the spins in a thin slice of the biological body. The G_z gradient on the last graphic (Fig. 2.7) accomplishes this.

Slice selection in MRI is the selection of spins in a plane through the object. The principle is explained by the resonance equation. Slice selection is achieved by applying a one-dimensional, linear magnetic field gradient during the period that the radio frequency (RF) pulse is applied. A 90^o pulse applied in conjunction with a magnetic field gradient rotates the spins that are located in a slice (or plane) through the object [6].

Consider the sample RF pulse sequence provided in Figure 2.7 [5]. When the magnetic field gradient, G_z, is originally applied, each slice through the biological body perpendicular to the *z*-axis is labeled by a definite frequency. Any plane

perpendicular to z can be chosen by using a selective RF pulse that has a center frequency matching that of the selected position on z, and the bandwidth determines the selected slice width along z. After the selective RF pulse, an entire plane of spins perpendicular to the z-axis is tipped into the xy direction; the precession of these spins creates the signal arising from the entire selected slice (initial tissue excitation). This isolates the chosen slice of the object for imaging, since all other parts of the body cannot give rise to any MR signal. At this stage there is no information about the contents of the slice since all spins have the same frequency. Once the slice has been selected, additional magnetic field gradients are applied across the slice in different directions (first G_y, then G_x series, in our case) in order to obtain the slice image data.

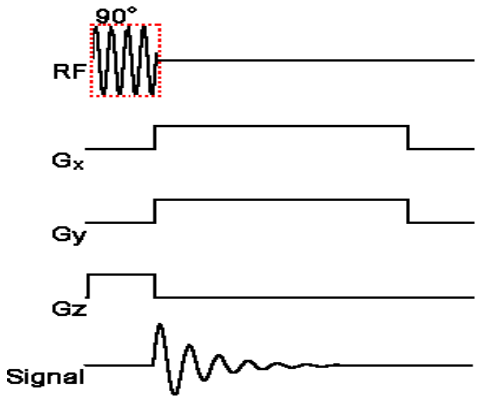

Figure 2.7: An Example of a Pulse Sequence for MR Signal Acquisition.

Then the decay of the excited tissue is observed ("listening" to the emitted signal) to fill the k-space corresponding to the spatial location of all the pixels located on the line in a given y -direction of the image of the chosen slice. The process is periodic, so we come back to the beginning of the RF pulse sequence for the next y-line acquisition until the k-space information is collected about all of the pixels of the selected slice in the object [7].

Figure 2.8 is a schematic representation of k-space gathered for the selected slice. After all of the k-space array elements for the particular slice of the object are filled, 2-D *iFT* is performed to translate the information from frequency to spatial domain. The outcome is a complete, reconstructed MR image of the selected slice in the z direction.

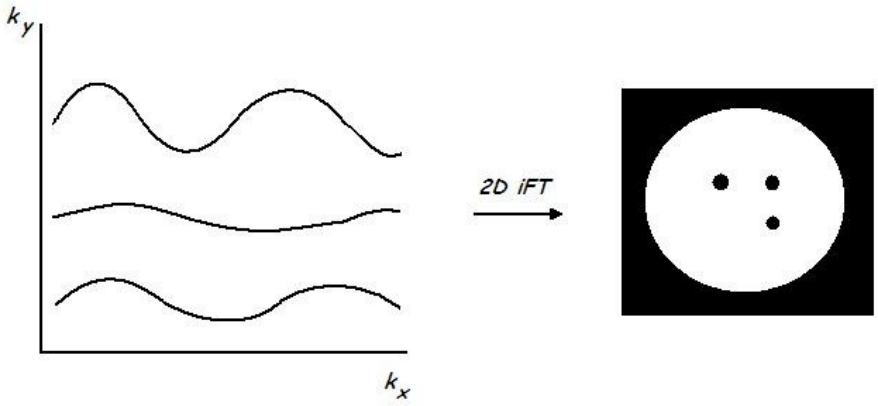

Figure 2.8: Schematic Representation of k-Space Array Transformed via 2-D *iFT* into an MR Image.

2.1.5 Tag Lines

In order to identify the medical pathology in the scanned object, sufficient contrast between the healthy and the diseased tissues is needed. As will be discussed in future sections, some stiff inclusions can be no different in the gray levels from those of normal tissue [8]. This lack of intensity contrast raises an issue when the motion evaluation is concerned. To address this issue, a technique known as tagging is used. In this technique, RF tagging pulses are used to spatially label an image with a specified physical or physiological property. Most commonly, a tagging pulse places a series of parallel stripes or orthogonal grids on an image. These stripes or grids are known as tag lines. An interesting feature of the tags is that they are being applied to the tissue once, and they are present throughout all the data acquisition process in sequential cinema-type imaging. This allows them to reflect all of the motion that originally occurs in the tissue. While the motion of the tissue occurs, the tag lines move (bend) in the same direction with the tissue itself. The deformation of the tags can be used later to evaluate the biomechanical properties of the imaged object [7].

Tags are typically applied as a magnetization preparation pulse prior to the actual imaging RF pulse sequence [1]. Virtually any imaging pulse sequence can be combined with a tagging pulse or a train of tagging pulses (Fig. 2.9). A gradient (known as a 'tagging gradient'*)* is generally required to produce the desired spatial pattern.

As the spatial patterns can be different for the applied tagging, the parameters for their application vary. Also, the width and frequency of their appearance (the number of lines per image) can be controlled. In this research the tag lines are applied in vertical, horizontal, and both directions simultaneously (grid).

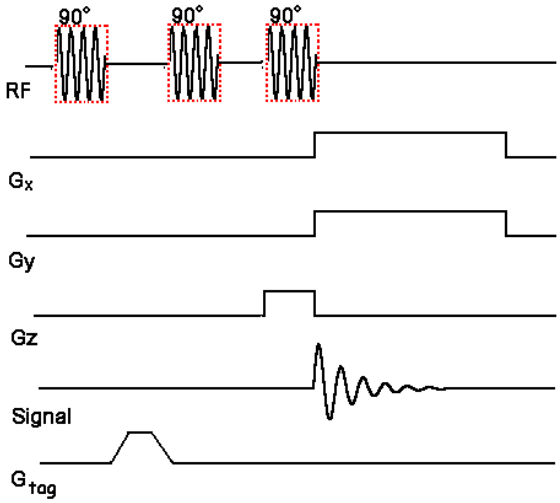

Figure 2.9: An Example of Image Acquisition Pulse Sequence with Tag Pulse.

2.2 Soft Tissue Elasticity Properties

Tissue elasticity properties convey important diagnostic information. Pathological tissues such as tumors of the breast or liver are 5 to 20 times stiffer than the surrounding healthy tissue [9]. This stiffening is a result of inflammation, dense cellular reactions, and highly cross-linked collagenous fibers. The increase in stiffness noted in these pathologic tissues provides unique bioelasticity contrasts for

disease diagnostics purposes. The existing methods to identify the stiff inclusions are manual *palpation* and *elastography*.

2.2.1 Manual Palpation

Palpation is an examination of the tissue by pressing on the surface of the body to feel the organs or tissues underneath; this is an effective technique that utilizes information about tissue elasticity properties. The idea of using simple palpation to detect this contrast is not new but is still effective. For example, most breast cancers are discovered by self-examination using manual palpation. Physicians also apply this technique to detect potential tumors in other soft tissues such as liver or prostate.

Figure 2.10 illustrates the principle of manual palpation [9]. The object consists of a soft medium shown in light grey and a stiff spherical inclusion (appears to be circular in 2-D) shown in dark grey. This can be considered a simplified model of a cross sectional view of a tumor embedded in normal tissue. If a compressive force is applied to the object, it will deform. However, the stiff target cannot be deformed as easily as the soft region. A constant compressive displacement deforms the region

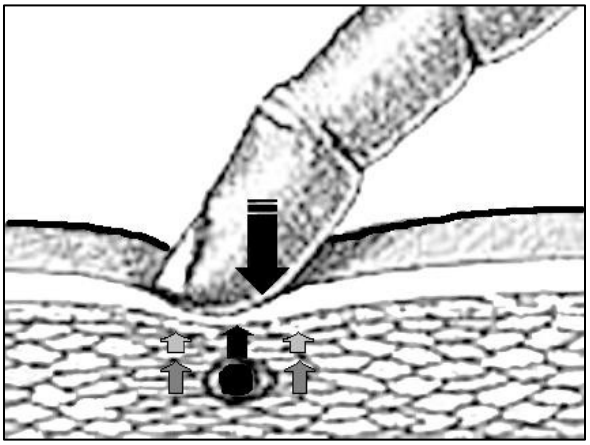

Figure 2.10: Manual Palpation [9].

above the stiff inclusion more than the adjacent regions [9]. Because the tissues are elastic, the more they are deformed, the greater counter force they generate. Thus, large stress builds above the inclusion because of large deformation. The fingers that displaced the surface also feel this stress distribution above the region that is being palpated. In the case shown in Figure 2.10, the fingers detect the stress difference, which leads to the discovery of a stiff object inside the tissue. Although the palpation is an effective technique for tumor or other stiffness detection [10, 11], it has some limitations in its usage: (i) only relatively large inclusions can be detected; (ii) the inclusion must be relatively close to the surface of the tissue; and (iii) the size and the stiffness of the inclusion cannot be reliably quantified. The major driving force behind the development of elastography was the need to overcome the limitations of the palpation method [10, 12].

2.2.2 Elastography

The term *elastography* applies to a broad range of parametric elasticity imaging in soft biological tissue, and an *elastogram* describes the spatial variations in the strain tensor components or reconstructed tissue bioelasticity (also called *viscoelasticity*, tissue stiffness, compliance, Young's elastic modulus, or shear modulus). Over the past few decades, there have been numerous investigations conducted to characterize the mechanical properties of biological tissue systems [13, 14]. Much of the work has focused on bone, dental materials, and vascular tissue. There are many articles that discuss methods used to characterize these tissues, and there is a large volume of experimental data on the mechanical response of these tissues to various types of

loading [15]. The stiffness parameter is a function of the elastic modulus of the tissue and its geometry and cannot be measured directly. A mechanical stimulus of some kind must be propagated into the tissue, and some precision means for detecting the resulting internal tissue motions must be provided. Such means include MRI or other diagnostic imaging modalities, including ultrasound imaging that can track minute tissue motion with high precision. Ultrasonic Elastography Imaging (UEI) uses an ultrasound transducer as a remote sensing device to scan the object before and after a compression is applied. A comprehensive literature review for UEI can be found in [16]. The main limitation of UEI is that the motion cannot be measured in arbitrary directions with equal sensitivity. Due to the limitation of ultrasound methods and the ability to overcome it by using MRI and unexplored nature, MRE is considered in this research because motion can be measured in all directions, including 3-D displacements.

2.2.3 Magnetic Resonance Elastography

Magnetic Resonance Elastography is an imaging technique for non-invasively assessing the elasticity properties of biological tissues using MRI. Although major contributions to elastography were initially made by the ultrasound community, the advantages of MRE have only recently been recognized. Initial studies demonstrated that this novel imaging technique has the potential to probe biological tissues effectively. MRE can provide estimates of the mechanical properties of tissues, such as shear modulus or Young's modulus [17, 18]. For example, small lesions of less than 1 cm in diameter and with stiffness only three times that of the background were

detected *in vivo* in human subjects [19]. While there are many possible applications of MRE, breast cancer detection and classification is currently the most common use. MRE has further potential as a diagnostic tool in such diseases as strokes, hyperthyroidism, disuse atrophy, or paralysis. A detailed description of multiple MRE methods is given in [17, 20, 21]. The technical task of MRE generally consists of the application of a deformation force, followed by tracking the tissue deformation (motion analysis). By the nature of the deformation force application, all the methods of MRE currently can be divided into *static* or *dynamic* techniques [22].

Static methods (or *quasistatic*) are characterized by applying quasistatic compression to the tissue and by estimating the resulting components of the strain tensor [8, 23]. Static approaches are best described as palpation by remote sensing. They are considered static because the data acquisition rate (frame rate) is much faster than the deformation rate. After producing an internal strain field, the object tissue is allowed to relax to reach equilibrium before measuring the displacement field. With these techniques, viscoelastic effects are generally ignored, making the reconstruction of the images easier.

Dynamic methods (also called *harmonic*) are characterized by applying periodic mechanical excitation at low frequencies (»250 Hz) to the tissue near the region of interest and inspecting the resulting tissue behavior by magnetic resonance. One or several "snapshots" of low-frequency shear wave propagation within the object are produced by controlling the relative phase differences between the mechanical

excitation and the motion-encoding gradients. The local displacement information in these images is then used as an input for an elasticity reconstruction algorithm.

While both dynamic and static techniques represent valid approaches to MRE, the dynamic methods have some limitations [8, 23]: shear-wave propagates in soft tissue at speeds of 1-20 m/s. A shear wave can require tens of milliseconds to traverse an object of small size (»30 mm), which may not be appropriate for studying small objects. The time to reduce the amplitude of the reflected waves can be much longer.

Dynamic measurements, which encode displacement during shear-wave propagation, are potentially inaccurate because of the interference of the primary shear wave with reflected or standing shear waves. To avoid these conditions, our research utilizes the static approach for the compression model. The general steps of the static MRE are as follows:

Step 1: Periodically compress the tissue.
Step 2: Acquire a series of tagged MR images at different time points of the compression cycle.
Step 3: Estimate the tissue motion on the images (image processing and analysis).

The details of implementation of each step specified above are provided in the following chapters.

Chapter 3
Mechanical Compression Instrument

Data acquisition in MRI involves spin dynamics where an imaging sequence applies repetitive RF pulses followed by listening to the echoes emitted from the sample. The received echoes are orchestrated to fill the *k*-space with the help of the gradient pulses. The compression device was expected to work in synchrony with this repetitious acquisition process and was furnished with a capability of applying compression periodically to induce motion on the underlying sample. In this regard, an essential operational feature and practical aspect of the device was to achieve a stable, repeatable, and uniform compression that would enable triggering the acquisition of the real MRI data. Such a device was not available commercially, and limited information existed about its construction to operate in a high magnetic field environment [24]. Interfacing the device to the scanner and making it work harmoniously with the tagged imaging sequence was another challenge and involved time-gating principles. Therefore, extensive learning and training were needed on how to operate the gating and monitoring system installed in the scanner for originally receiving the vital signs of live animals while being scanned. Another unique desirable feature of the device was that it had to be able to comfortably accommodate small animal oncology models for future research.

In this chapter, these issues concerning the drafting of a practical device are addressed and a final successfully working prototype is introduced. The chapter is organized as follows: Section 3.1 introduces the design of the instrument and gives a diagrammatic look at its components. Section 3.2 describes the implementation of the

prototype, and Section 3.3 details how the compression of the device was monitored and how this information was relayed to the scanner for the gating purposes.

3.1 Design

The requirements for the design of the compression device were first outlined to meet the following criterions.

Overall: The device should be light weight and must fit into an experimental 9.4 T MRI scanner with a 12 cm inner diameter gradient coil where a 7 cm inner diameter volume coil was inserted. The available space for inserting the compression device was therefore a 7 cm diameter cylindrical volume.

Material: Due to the magnetic field of the MRI scanner, the instrument had to be made of non-magnetic material.

Compression: The compression induced by the device had to be uniform, periodically repetitive, and stable over time. This requirement was introduced because tagged MRI protocol involves gated-data acquisition.

Size: Since an immediate application was in mind for the animal research in the future, the device had to be able to accommodate small laboratory animals, particularly mice, since this animal model allows tumor cells to be implanted into its mammalian gland for further growth. Therefore, the hardware had to be adjustable to hold different sized animal oncology models or phantom samples ranging from 1 to 5 cm in length.

In compliance with the above requirements for the hardware design, a compression device depicted in Figure 3.1 was first drafted as a blue print and

dimensions were then decided. Based on this information, a prototype was constructed.

Figure 3.1. Original Draft of the Prototype Compression Device.
Components identified by numerals.
I - Electromagnetic coil to produce angular motion.
II - Pin.
III - Gear assembly to transfer circular motion to linear motion using teethed bar.
IV - Teethed bar was allowed to slide horizontally.
V - Compression plate was attached to the end of the pole to deform the sample.
VI - Sample with an inclusion was placed on a slick surface.
VII - Fixed plate supporting the sample against the applied compression.

3.2 Prototype

The prototype (Fig. 3.2) was built according to the design in Figure 3.1. Several iterations took place to reach its finalized form. All real data acquisitions were conducted using this prototype device. Note that the MR volume coil (X) was also included in Figure 3.2 to clearly show the positioning of the device into the coil.

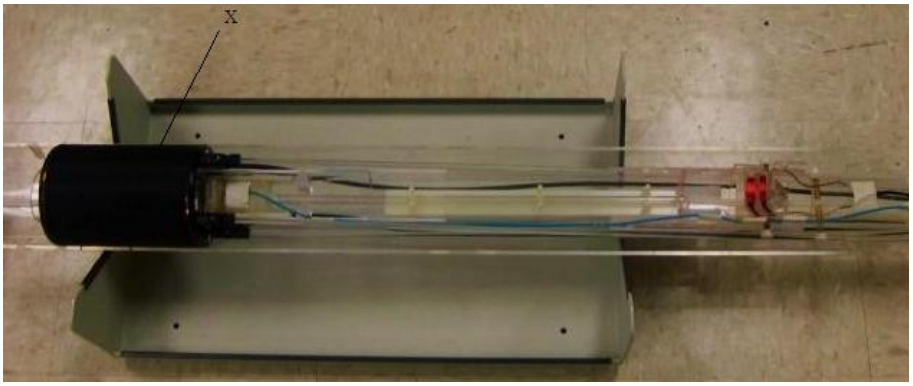

Figure 3.2: Implementation of Prototype Compression Device.
X points to a Volume coil.

The prototype device consisted of a hollow tube made of Plexiglas (MRI-safe material). It was cut in half along its axis and housed two main components inside: a motion generator and a sample holder.

The motion generator consisted of an electro-magnetic coil (I) and gear assembly, as shown in Figure 3.3. The coil was formed by winding 50 turns of 18 gauge insulated wire on a 3 cm x 6 cm rectangular piece of Plexiglas, which was carved at the edges to hold the wires. A plastic circular gear (III) was mounted inside this piece, and both were attached to the tube by a strong and durable nylon pin (II). A teethed bar (IV) was passed through the opening in the center of the rectangular piece and engaged with the gear. When placed in a strong magnetic field of 9.4 T and energized by bipolar pulses delivered across its terminals, the coil's internal magnetic field interacted with the external magnetic field. This interaction forced the coil to reorient itself depending on the polarity of the applied voltage.

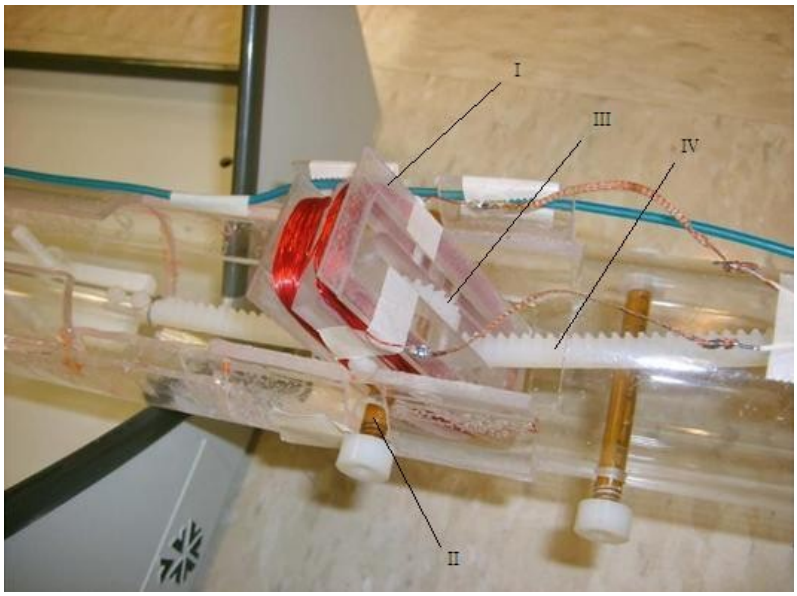

Figure 3.3: Motion Generator of Compression Device.
Components identified by numerals.
I - Electromagnetic coil.
II – Nylon pin.
III – Plastic circular gear.
IV - Teethed bar.

The reorientation prefers a minimum energy state where the internal and external magnetic fields are aligned in the same direction. The circular flip motion during the reorientation is converted to a linear motion by the gear assembly that slides the teethed bar back and forth and subsequently delivers the motion to the compression plate attached to the bar.

To drive the electro-magnetic coil, we used a 4017A 10 MHz Sweep Function Generator (BK Precision Yorba Linda, Ca) that was capable of producing functions with frequencies between 0.1 Hz and 10 MHz. The output of this generator could be set to either Sinusoidal, Square, Triangle, Pulse, or Ramp waveform that would run

periodically. We examined square and triangular waveform settings while changing the frequency from 1 and 10 Hz and the peak amplitude from ±1 to ±5 V. Depending on the compliance of the sample being studied, different settings for the frequency or voltage were used to induce the desired motion in the sample.

The sample holder is shown in Figure 3.4. The phantom or the biological tissue sample with or without the embedded stiff inclusion (or tumor) and with affixed on top the pneumatic pillow (I) was placed within the opening (II) and secured between the compression plate (III), fixed plate (IV), and the wall of the Plexiglas tube. The compression plate was allowed to move freely with no friction, and its motion was dictated by the sliding bar. The movement of the compression plate squeezed the sample against the fixed plate at the other end. The configuration seen in the figure describes the boundary conditions "stress free."

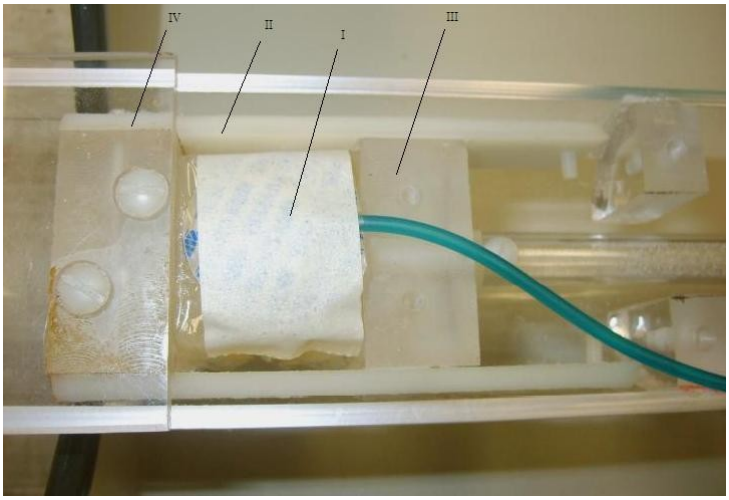

Figure 3.4: Sample Holder of Compression Device.
Components identified by numerals.
I - Tissue sample with affixed on top pneumatic pillow.
II – Opening.
III – Compression plate.
IV - Fixed plate.

3.3 Compression Monitoring

In principle, the output from the function generator could be used to assess the compression of the sample and ultimately to trigger the scanner. However, this process required additional hardware development. Considering the difficulty in predicting the time delays between the output signal and the compression experienced by the samples with different compliances, we opted to use a MR-compatible Small Animal Monitoring and Gating System (Model 1025, SA Instruments, Inc., NY) that was readily available and used regularly with the scanner. As indicated above, the externally introduced compression on the sample during the MR acquisition was a periodic process similar in its qualities to those seen during a physiological vital sign of respiration. This similarity provided a strong justification for monitoring the compression by using the same principles of respiration monitoring and gating in living animals being scanned. The monitoring system was originally designed specifically to meet the physiological monitoring and gating needs for anesthetized animals in the MR environment. The system consists of data acquisition modules located near the animal (agar phantom or biological samples in the context of this research). The control/gating module connected to a Personal Computer (PC) located near the operator console. The PC displayed multiple waveforms that represent measured respiration values read by the sensors of the pneumatic pillow, estimated trends, and produced gating pulses. The sensory modules were controlled by menu-driven software from the PC.

The respiration module resided just outside the magnet bore. Respiration was measured using a small pneumatic pillow (Fig. 3.5) that was attached to the sample (in our case, the phantom). The control/gating module received data from the acquisition modules using optical fibers. The module sent data to the PC for display and received instructions from the PC to control measurement and gating functions. Respiratory gates were generated by the control/gating module's microprocessor and sent to the MR system.

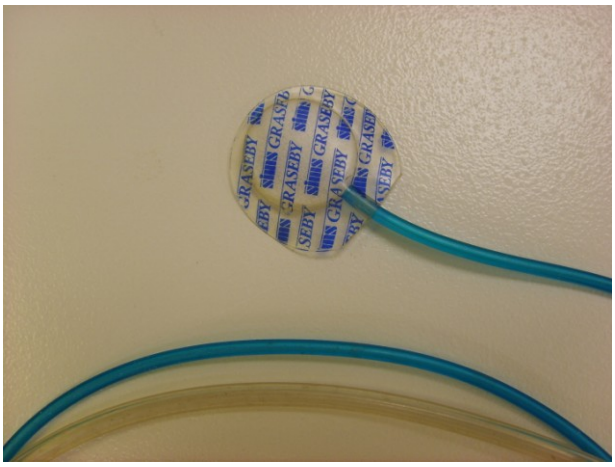

Figure 3.5: Pneumatic Pillow.

Figure 3.6 depicts a sample process of monitoring the compression that was produced by the monitoring instrument during one of the agar phantom data acquisitions. The compression was being monitored at all stages during the data acquisition process. As seen in the figure, the compression was periodic and stable over the indicated time frame. The peaks of the cycle show the highest points of the compression of the sample, and the lower points display the decompression. The

gating of the process was performed while the compression was monitored. A proper gating was required for a successful MR data acquisition. Each period was divided into phases, and number of frames in the MRI sequence was set a priori according to this division. After the triggering, MR data were gathered sequentially for each phase. The MRI sequence also allowed introducing additional time-delay between the trigger signal and the start of the acquisition. However, this feature was not used in this research.

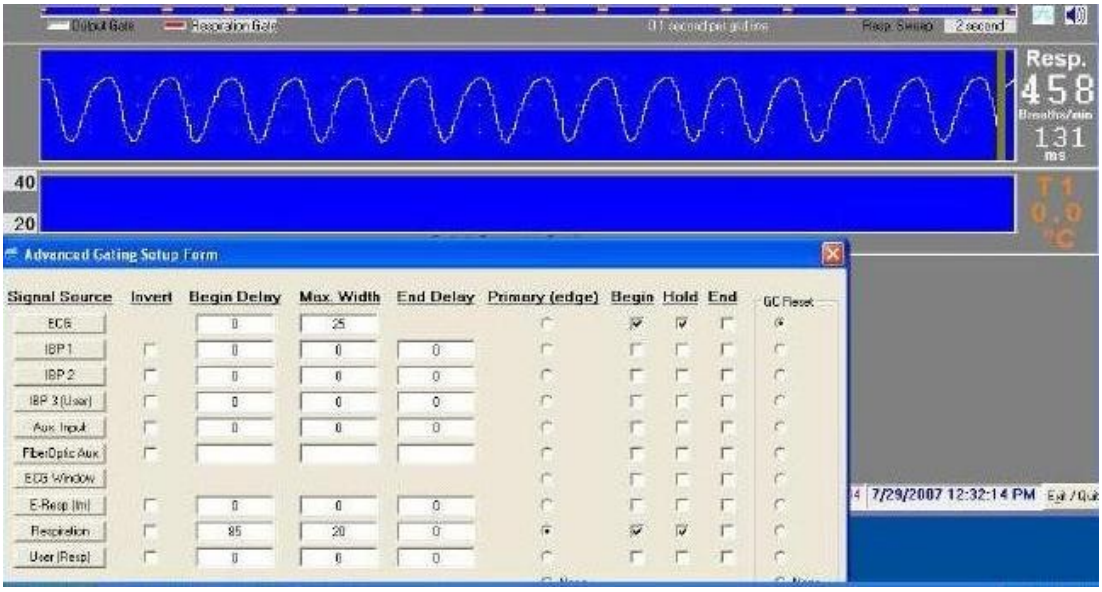

Figure 3.6: Screenshot of Compression Monitoring.

Figure 3.7 shows a screenshot of the scanner's computer window after displaying the sequential tagged images acquired from a uniform phantom. This acquisition involved 20 frames within the full period, spanning both the compression and decompression phases. Note that the sizes of images in horizontal and vertical

directions change due to the applied compression. The other parameters of the data acquisition are provided in Section 4.2.1.

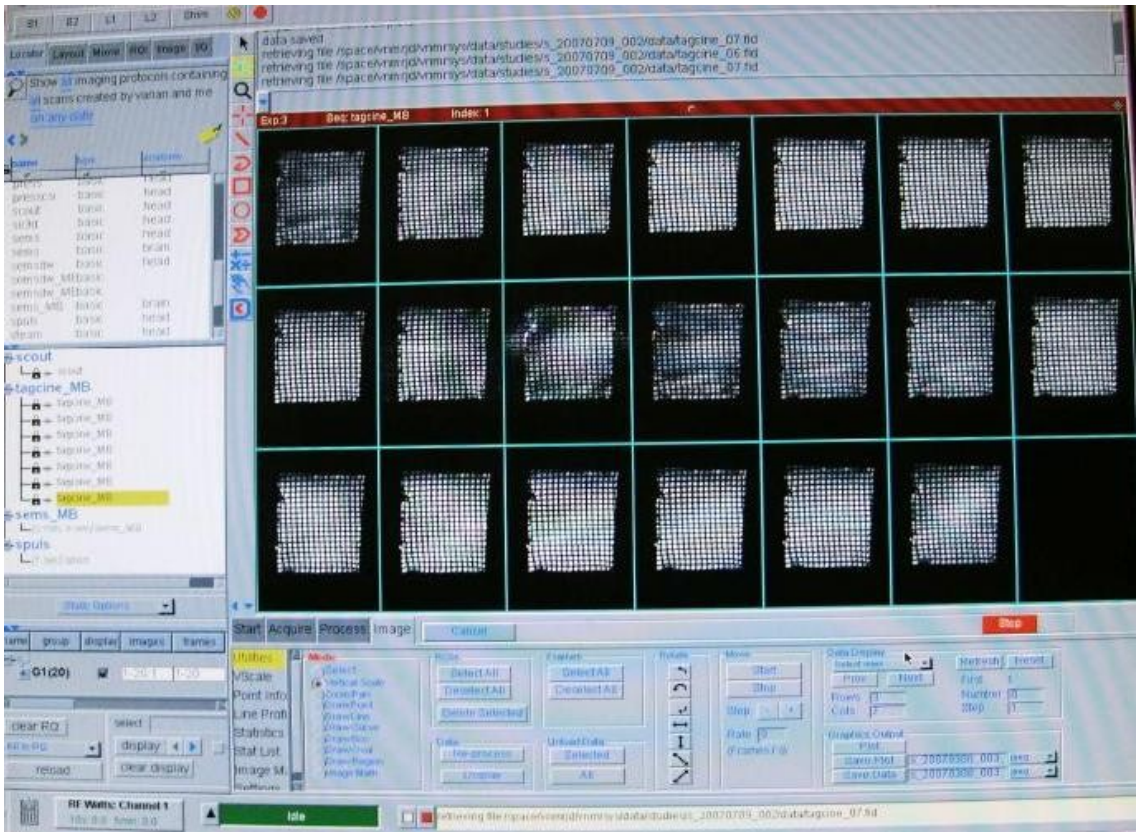

Figure 3.7: Screenshot with Sample MRI Data Acquisition.

Chapter 4
Experimental Procedures for Generating Data

In this chapter, the experiments that were performed for generating both synthetic and real data are described. The chapter is organized as follows: Section 4.1 provides information regarding synthetic data, and Section 4.2 shows the process of preparation and the features of the agar phantoms with details about how the experiments for gathering real data from the phantoms were performed.

4.1 Synthetic Data

Synthetic tagged images were generated using numerical simulations of signal, noise, and motion to systematically test the performance of the implemented OF algorithm under controlled settings. The simulated motion constituted the true motion field that was used as a benchmark reference for comparing the motion estimates [25]. This allowed us to quantitatively assess the performance of our OF-based motion estimator. Images embedded with motion and degraded by signal independent Gaussian noise were generated using software written in Matlab programming language (Mathworks, Inc., Natick, MA) [26]. Relevant Matlab codes to produce these images are provided in the Appendix.

For the purpose of proving the concept, the first simulation set was kept very simple. A square image with tag lines was initially synthesized. Motion encoded noisy images were obtained by spatially shifting this image and introducing a different amount of noise.

This set of images was instrumental in understanding the dependence of the performance of the OF algorithm on the translational motion and noise level under

otherwise identical conditions. We considered a synthetic tagged image of a square size in 40 pixels x 40 pixels and tag lines applied in both horizontal and vertical directions with the spacing of 10 pixels.

The image consists of a gray scale intensity variation. To introduce the intensity variation (speckles), we applied a small amount of white noise to the original square and then smoothed the composition with a Gaussian filter (to make the noise more evenly distributed). In the next step, the tag lines were simulated. To do so, we created a 2-D Gaussian window with the size of 10 pixels x 10 pixels and a standard deviation of 1.5 pixels and convolved it with the speckled square. The result was an original image similar to the real experimentally acquired tagged MRE data. Formation of the image step-by-step is given in Figure 4.1.

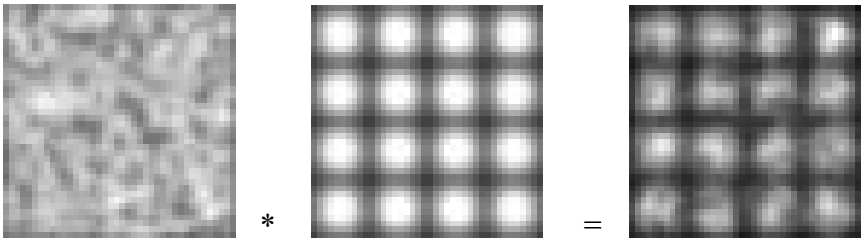

Figure 4.1: Tagged Speckled Square Image Formation (left to right): Speckles generated; Tag lines grid; Tagged Speckled Square Image.

After the original image was formed, it was rigidly translated diagonally by 1, 2, and 3 pixels. The original images and the resulting versions from the translations are shown in Figure 4.2.

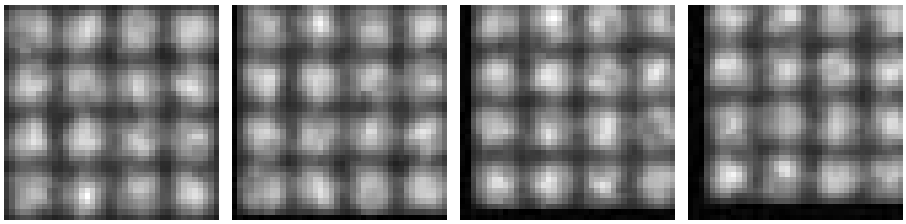

Figure 4.2: Series of Translated Square Images with Tag Lines (left to right): Original Image; Square translated diagonally by 1 Pixel; Square translated diagonally by 2 Pixels; Square translated diagonally by 3 Pixels.

To make our simulation data as close as possible to the real experimentally acquired tagged images, we introduced signal independent noise to each original and translated images individually. We generated random white noise in 2-D and smoothed the realization by a 2-D Gaussian filter. Since the task was to test our OF algorithm's sensitivity to the amount of noise introduced, we generated a set of pairs of the original and the translated images with different amounts of noise. The sample pair is provided in Figure 4.3. As can be seen, there are two images, original and translated diagonally by 1 pixel, with the multiplicative noise coefficient 0.05.

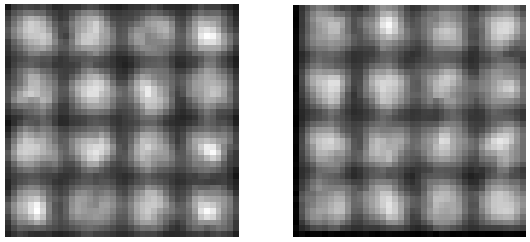

Figure 4.3: A Pair of Original Speckled Square Image (left) and its Translated Diagonally by 1 Pixel Version (right). Noise Coefficient = 0.05.

In mathematical terms, image formation for this simulation data can be written as

$$I_1(x,y) = I_0(x,y) + \alpha \cdot n_1(x,y)$$
$$I_2(x,y) = I_0(x - x_0, y - y_0) + \alpha \cdot n_2(x,y) \qquad (4.1)$$

where $I_0(x,y)$ is an original noise-free intensity image with tags and speckles, $I_0(x - x_0, y - y_0)$ is a shifted noise-free intensity image with tags and speckles, n_1 and n_2 are two different realizations of a signal-independent noise model, α is the noise constant, and $I_1(x,y)$ and $I_2(x,y)$ are original and shifted images, respectively, with the noise added.

The second simulation set involved a cylindrical inclusion contained in a homogeneous background, as shown in Figure 4.4. The background of the image represents a healthy tissue that is being compressed normally, and the circular insertion models a tumor or a region of suspected cancerous growth that is stiff. Again, the contrast between the target and the background were left unchanged. We considered the plane strain condition and utilized the analytical formulas provided in [27] for the profiles under the uniform loading from the top and bottom boundaries.

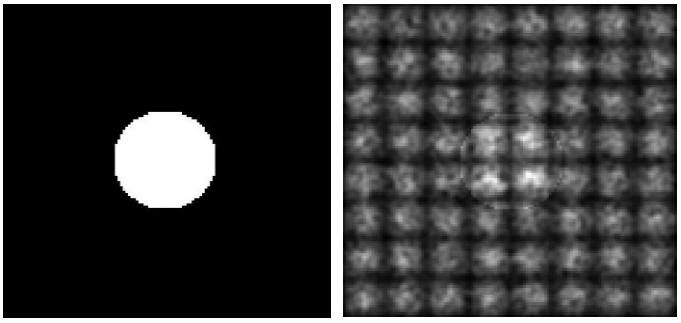

Figure 4.4: Images with 2-D Cylindrical Inclusion and Tag Lines (left to right): 2-D cylindrical inclusion simulation; Speckled image with inclusion and tag lines.

According to cylindrical geometry, the motion of each pixel in a series of two or more consequent images can be described by u_r that denotes radial direction, and u_θ – a radial angle.

To create a motion profile for compression of media that includes a stiff 2-D cylindrical inclusion, two sets of motion parameters should be defined: u_r and u_θ inside the boundary of inclusion, as well as u_r and u_θ outside of the boundary.

To simplify formulas provided later, we introduce the following constants:

$$b = -2\frac{(m_i - m_m)}{(m_m + m_i k_m)}$$

$$g = \frac{(\, m_m(k_i - 1) - m_i(k_m - 1)\,)}{(\, 2m_i + m_m(k_i - 1)\,)}$$

$$d = \frac{(m_i - m_m)}{(m_m + m_i k_m)}$$

$$b_0 = \frac{m_i(k_m + 1)}{(\, 2m_i + m_m(k_i - 1)\,)}$$

$$g_0 = 0$$

$$d_0 = \frac{m_i(k_m+1)}{(m_m+m_i k_m)} \qquad (4.2)$$

where m_m is shear modulus for the media, m_i is shear modulus for inclusion, k_m is bulk modulus for media, and k_i is bulk modulus for inclusion.

Then, using (4.2), for each point (r, θ)

- outside of inclusion (media)

$$u_r{}^m(r,\theta) = -\frac{T}{8m_m r} \cdot ((k_m - 1)r^2 + 2ga^2 + (b(k_m + 1)a^2 + 2r^2 + 2d\frac{a^4}{r^2}) \cdot cos2\theta)$$

$$u_\theta{}^m(r,\theta) = \frac{T}{8m_m r} \cdot \left(b(k_m - 1)a^2 + 2r^2 - 2d\frac{a^4}{r^2} \right) \cdot sin2\theta \quad (4.3)$$

- inside the boundary of inclusion (inclusion):

$$u_r{}^i(r,\theta) = -\frac{Tr}{8m_i} \cdot \left(b_0(k_i - 1) + \left(g_0(k_i - 3) \cdot \left(\frac{r}{a}\right)^2 + 2d_0 \right) \cdot cos2\theta \right)$$

$$u_\theta{}^i(r,\theta) = -\frac{Tr}{8m_i} \cdot \left(g_0(k_i + 3)\left(\frac{r}{a}\right)^2 - 2d_0 \right) \cdot sin2\theta \quad (4.4)$$

where T is the applied stress from the top and bottom boundaries, and a is the radius of the inclusion.

During the compression, the left boundary was fixed and the upper and lower boundaries were allowed to slide freely. The $u-$ and $v-$maps upon compression are depicted in Figure 4.5.

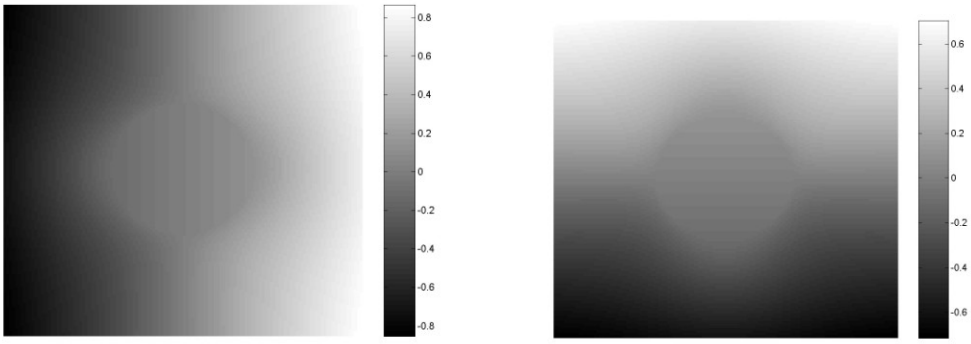

Figure 4.5: $u-$ and $v-$Maps for Image with 2-D Cylindrical Inclusion (left to right, respectively).

4.2 Real Data

The research considered real data from two types of samples: phantoms with and without a cylindrical inclusion. The samples were prepared using different

concentrations of agar (or gelatin) home-made samples. The phantoms were constructed as $3 \times 3 \times 3\ cm^3$ blocks to quantitatively simulate mechanical properties of a soft biological healthy tissue and one with a tumor. While the first type of phantoms had no inclusion present, the second type contained a hard inclusion of cylindrical shape placed at the center of a uniform background. The inclusions had a shear modulus value of 40 kPa (that is a typical value for malignant tumors), while the background was at 10 kPa. To make such a phantom, two batches of gel were prepared separately for the background and inclusion by varying the concentration of agar (3 to 6%). The gel mixture for the inclusion was poured into cylindrical or spherical molds with a 5 mm radius and cured for 2 hours at room temperature. Next, the batch of gel mixture was prepared for the background. The inclusion was removed from the mold and suspended in a rectangular container that was then filled with the second batch of gel. Each sample contained only one inclusion (Fig. 4.4). Since we cannot clearly see the stiff cylindrical inclusion on the picture due to lack of contrast between the two batches of agar with different concentrations, it is schematically shown on Figure 4.6 with a red circle. In order to hold its shape, each phantom is wrapped in clear plastic.

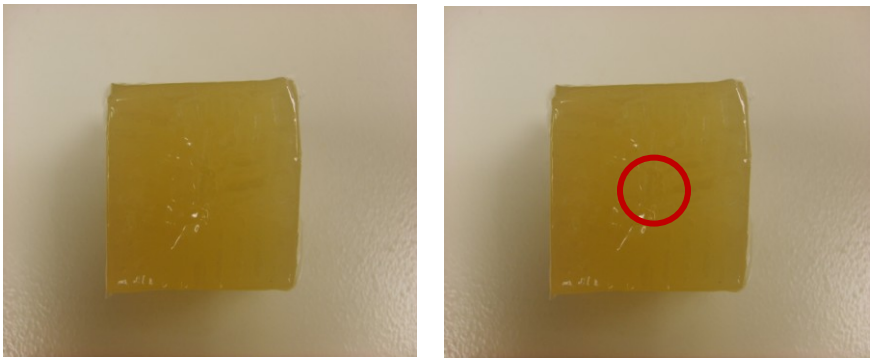

Figure 4.6: Agar Phantoms without and with the Stiff Cylindrical Inclusion (left to right, respectively). Radius of inclusion r = 5 mm.

4.2.1 Experimental Data Acquisition from Phantoms

As described above, our ready phantoms were wrapped in a thin layer of plastic film. The respiration pneumatic pillow was tightly fixed on the top of the sample using self-adhesive tape. The compartment size of the MRE compression device was adjusted to the size of the sample, and then the phantom was loaded into the compartment. It was important to make sure there was no space left between the phantom and the walls of the sample holder so that no or minimal friction is created during the data acquisition associated with the improper spacing of the phantom. This was difficult to control during the experimental data gathering for this research due to the design of the sample holder chamber. To improve that, some modifications will be introduced to the design of the compression device as a part of future work.

We used the volume RF coil with a 7 cm inner diameter for data acquisition. In order to successfully acquire data, the coil had to be positioned around the chamber of the MRE compression device with the sample inside so that the center of the sample

coincided with the center of the coil. Following that, our compression device with the coil was then fitted and fixed inside a positioning slot for MRI experiments. For the positioning slot, we used a half tube of non-magnetic material with a 12 cm diameter. This size was chosen in consideration of the inner diameter of the MRI bore and the experimental hardware setup size. Some minor adjustments had to be made in order to buffer possible motion of the device inside the MRI scanner during data acquisition. The adjustments were made using non-magnetic materials and self-adhesive tape.

The next procedure of the experimental setup was to perform the rough tuning of the volume coil. The coil was connected to the coil tuner. By alternatively manipulating the two sets of poles of the tuner, the coil was calibrated to operate at 400 MHz.

After preliminary preparations were performed, the device was ready to be placed in the magnet bore of the MRI scanner. It had to be positioned inside the scanner so that the sample was located precisely in the middle of the bore (at the isocenter of the scanner) and the coil of the compression device was located at the periphery. The wave generator was connected to the coil of the device. The next step was to perform the final tuning of the volume RF coil.

Testing of the positioning in the bore of the MRI scanner of our setup was performed using the predefined pulse sequence “scout” with the following parameters: minimal TE = 1.88, Data Matrix = 128 x 128, Readout = 100, Phase = 100, Slices = 1, Thickness = 2. As the result, three images were acquired: axial,

coronal, and sagittal projections of one slice located in the middle of the scanned sample.

As the next stage of the experimental setup, we tested the gating system and chose the parameters for the compression monitoring. For this purpose, we generated a sinusoidal electromagnetic wave with the frequency of 7 Hz using the wave generator. This produced the compression of our sample. The motion was captured by the registration/ECG pillow and was transferred to the monitoring system. Due to the close monitoring of motion, we could reliably define the needed gating parameters for our experiments. The parameters were as follows: TR = 300, TE = 1.88, Flip Angle = 30, Readout = 40, Phase = 40, Receiver Gain = 10, Frames = 10, R-R Interval = 130, Tag Line Width = 1.00, Tag Line Spacing = 3.00. The experiment was performed with the "tagcine_MB" pulse sequence written in our laboratory specifically for the tagged cardiac MR images acquisition using a 9.4 T MRI scanner.

The parameters of the acquisition were changing in order to obtain images with different features: different projections of the same phantom, different parameters of tag lines patterns, different resolution on the images, etc. As we performed experiments, the compression was instantly monitored and the needed adjustments in experiment configurations were done in real time. Depending on the parameters, each experiment took approximately 7 minutes.

Chapter 5
Motion Analysis

The goal of a motion analysis is to describe the change in the position of a moving body that occurs between two images. Algorithms are developed for handling global motion problems such as rigid motion (translation, rotation) or alignment of images from different imaging modalities (CT, MRI, and mammogram). This type of algorithms accomplishes registration [28]. Other techniques consider local motion, which occurs when the motion shows dependence on the underlying specific region of the image. Optical Flow (OF) algorithms were developed to analyze such motion.

This chapter provides information on motion analysis techniques and their evaluation methods. Section 5.1 introduces the concept of OF techniques and gives an explanation of the algorithms that were implemented, tested, and optimized in applications to MRE data in this research. The errors that were calculated and used as an evaluation tool for the performances of the OF algorithms are described in Section 5.2.

5.1 Optical Flow

Optical Flow is a technique used to compute an approximation to the 2-D motion field -- a projection of 3-D velocities of surface points onto the imaging surface from spatiotemporal patterns of image intensity. In mathematical terms, the OF at the pixel (x, y) is a 2-D velocity vector as an approximation to the real motion:

$$(u, v) = \left(\frac{dx}{dt}, \frac{dy}{dt}\right) \quad (5.1)$$

The fundamental assumption in the OF approach is that the brightness intensity function of the moving object remains approximately constant at least for a short duration of time [29]. That is

$$I(x, y, t) = I(x + dx, y + dy, t + dt) = I(x + u, y + v, t + 1) \quad (5.2)$$

Here I represents intensity, (x, y) are spatial coordinates, and t is time variable. The major stages of processing in OF are as follows [25]:

(1) Prefiltering or smoothing with low-pass/band-pass filters (to extract signal structure of interest and enhance SNR);

(2) Extraction of basic measurements such as spatiotemporal derivatives (to measure normal components of the velocity) or local correlation surfaces;

(3) Integration of the previously extracted measurements to produce a 2-D flow field.

5.1.1 Differential Techniques

There are different ways to calculate the velocity field [30]. After a literature review, we chose differential OF techniques for their simplicity and reliability.

The differential technique was introduced for calculating the velocity in two consecutive images [29]. The approach uses a linear constraint in the space spanned by horizontal and vertical components of the velocity vectors known as Optical Flow Constraint (OFC). This constraint relates the spatial and temporal $\frac{I}{t}$ derivatives of the image brightness function at each point to the velocity vectors u and v, at that point. Since there is only one equation and two unknowns, this equation cannot be solved for both horizontal and vertical components of the OF without additional assumptions

or information. In other words, a single equation produced by OFC only constrains the solution vectors (u, v) to lie on a constraint line in 2-D u-v-space: we need at least one other non-parallel constraint line to uniquely determine the flow. Various alternative strategies have been suggested, but regardless of the strategy, we usually arrive at a set of linear equations to solve for the optical flow at each point.

Requirements for differential techniques are that $I(x, y, t)$ must be differentiable and the image intensity must be nearly linear. In general terms, the flowchart of OF estimation using differential methods can be described as follows:

Input: Sequence of images

Output: Difference between the images (velocity flow)

Step 1: Filter each image (to suppress noise)

Step 2: For each pixel in the images

Step 2.1: Compute the matrix of spatial image gradients and the vector of partial temporal derivatives of the image brightness

Step 2.2: Compute image flow in both *x*- and *y*- directions

Step 2.3: Mark each point with an arrow

Step 2.4: If the point's flow magnitude is larger than a threshold, indicate its flow

Step 3: Visualize the flow

As follows from [30], differential techniques produce the best results based on their accuracy and density of velocity estimates in motion analysis from an image sequence.

One of the primary goals of this research was to develop and test a robust and effective algorithm for motion analysis that will be used for motion analysis in tagged MRI with high accuracy and noise insensitivity. Based on the literature review and our preliminary investigations on the performance and complexity of the current approaches, the following OF algorithms were implemented and evaluated using simulation and experimental based data.

- One-step differential technique [31];
- Iterative differential technique of [29].

5.1.2 One-step OF Method

The One-step method uses a weighted least-squares fit of local first-order constraints to a constant model for velocity estimates (u, v) in each small spatial neighborhood Ω by minimizing

$$\sum_{x\in\Omega} W^2(x,y)[\nabla I(x,y,t) \cdot (u,v) + I_t(x,y,t)]^2 \qquad (5.3)$$

where gradient $\nabla I(x,y,t) = (I_x(x,y,t), I_y(x,y,t))^T$, $I_t(x,y,t)$ is the partial time derivative of $I(x,y,t)$, and $W(x,y)$ denotes a window function that gives more influence to constraints at the center of the neighborhood than those at the periphery. The solution to (5.3) is given by

$$A^T W^2 A\,(u,v) = A^T W^2 b \qquad (5.4)$$

where for n points $x_i \in \Omega$ at a single time t,

$$A = [\nabla I(x_1, y_1), \dots, \nabla I(x_n, y_n)]^T$$

$$W = diag[W(x_1, y_1), \dots, W(x_n, y_n)]$$

$$b = -(I_t(x_1, y_1), \dots, I_t(x_n, y_n))^T \quad (5.5)$$

The solution to (5.4) is

$$(u, v) = [A^T W^2 A]^{-1} A^T W^2 b \quad (5.6)$$

which is solved in closed form when $A^T W^2 A$ is nonsingular, since it is a 2 × 2 matrix

$$A^T W^2 A = \begin{bmatrix} \sum W^2(x,y) I_x^2(x,y) & \sum W^2(x,y) I_x(x,y) I_y(x,y) \\ \sum W^2(x,y) I_y(x,y) I_x(x,y) & \sum W^2(x,y)\, I_y^2(x,y) \end{bmatrix} \quad (5.7)$$

where all sums are taken over points in the neighborhood **Ω** [30-32].

5.1.3 Iterative OF Method

The Iterative OF method combines the gradient constraint with a global smoothness term to constrain the estimated velocity field (*u, v*), minimizing

$$\int (\nabla I(x,y,t) \cdot (u,v) + I_t(x,y,t))^2 + \lambda^2 (\left|\left|\nabla u\right|\right|_2^2 + \left|\left|\nabla v\right|\right|_2^2)\, dx\, dy \quad (5.8)$$

defined over the domain D. $\lambda^2 \left(\left|\left|\nabla u\right|\right|_2^2 + \left|\left|\nabla v\right|\right|_2^2\right)$ is a smoothness constraint. Magnitude of λ reflects the influence of the smoothness term.

We obtain image velocity by minimizing (5.8) via solving iterative equations

$$u^{k+1} = \bar{u} - \frac{I_x[I_x \bar{u}^k + I_y \bar{v}^k + I_t]}{\lambda^2 + I_x^2 + I_y^2}$$

$$v^{k+1} = \bar{v} - \frac{I_y[I_x \bar{u}^k + I_y \bar{v}^k + I_t]}{\lambda^2 + I_x^2 + I_y^2} \quad (5.9)$$

where *k* denotes the iteration number, and $\bar{u}$ and $\bar{v}$ are neighborhood averages of u^k and v^k.

Since we are using two consequent images, our time is considered as 1 unit, and our velocities u and v in fact represent displacement of the same pixel [29, 30].

5.2 Error Analysis

One-step and Iterative OF algorithms were tested on synthetically generated and experimentally acquired phantom data. The performances of the methods were compared quantitatively using criteria of angular error (AE) and vector length error (VLE) between the estimated values of (u, v) by OF and their corresponding true values (u_{true}, v_{true}) from the numerical simulations [25]. Note that true values from the phantom studies were not available.

Angular error was calculated as

$$AE = \cos^{-1}\left(\frac{u \cdot u_{true} + v \cdot v_{true}}{\sqrt{u^2+v^2} \cdot \sqrt{u_{true}^2+v_{true}^2}}\right) \tag{5.10}$$

Vector length error was calculated according to

$$VLE = \sqrt{u_{true}^2 + v_{true}^2} - \sqrt{u^2 + v^2} \tag{5.11}$$

Chapter 6
Results and Discussion

In this chapter, the results of our research are provided. Section 6.1 considers the outcomes of the synthetic data experiments with the simple translational motion. Section 6.2 illustrates the results for the simulations of the soft media with a stiff 2-D cylindrical inclusion. Details of the experiments with the agar phantoms without an inclusion and with a stiff cylindrical inclusion embedded in the center of the soft media are given and discussed in Sections 6.3 and 6.4, respectively.

6.1 Simple Translational Motion

Figure 6.1 shows typical synthetic noise-free tagged images representing purely translational type motion diagonally by 1 pixel. The size of the images was 40 pixels x 40 pixels, and the tag line spacing was 10 pixels in both directions. Motion estimates from the images were obtained by using One-step and Iterative OF algorithms. Quivers were drawn for the true motion profile as well as the results for the motion estimates from both algorithms, and all three are displayed in Figure 6.2. The true motion vectors appear in blue, and the estimates by One-step and Iterative algorithms are represented by flow vectors with red and green colors, respectively. The window size was set to 5 pixels x 5 pixels in the One-step algorithm, which resulted in no estimates for the 2 pixels at the edges surrounding the flow map, and hence the estimates were produced over 36 pixels x 36 pixels. The Iterative algorithm was run with 1,000 iterations, and the smoothness parameter was set to $\lambda = 100$. The lengths of the vectors in the figures were scaled by ¾ for better visualization of the flow maps. All vectors were also plotted jointly. The magnified

version within a central region of the joint display of the flow map in Figure 6.2 is provided in Figure 6.3 to clearly display the typical behaviors of the vectors. From the flow maps, it is visually evident that for the given data parameters, both algorithms perform relatively well, and the estimated motion vectors closely match the true motion when the images are noise-free. This is further supported by the quantitative error calculations from Eq. 5.10 and Eq. 5.11: AE = 0.83˚ and VLE = 0.03 pixels for the One-step algorithm and AE = 1.05˚ and VLE = 0.04 pixels for the Iterative OF algorithm, both computed over a square section centered from pixels 5 to 35 in both directions. Small AE values mean that the estimated flow vectors are aligned along the same direction with the true motion vectors. The small VLE value indicates that the estimated flow vectors have nearly the same lengths as the true motion vectors. The corresponding error results when the noise-free image was translated by 1, 2 and 3 pixels diagonally are given in Table 6.1. When the true motion increases, the performance of both estimators degrades as indicated by the increased error results in both the angle and length values.

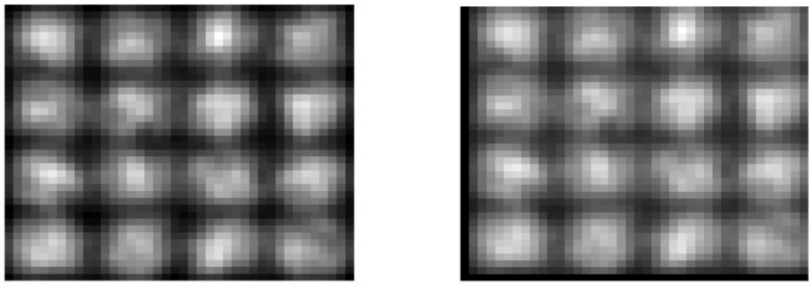

Figure 6.1: Original Noise-Free Image (left) and its Translated Diagonally by 1 Pixel Version (right). These two images constitute a pair for estimating flow vectors representing motion using One-step and Iterative OF algorithms.

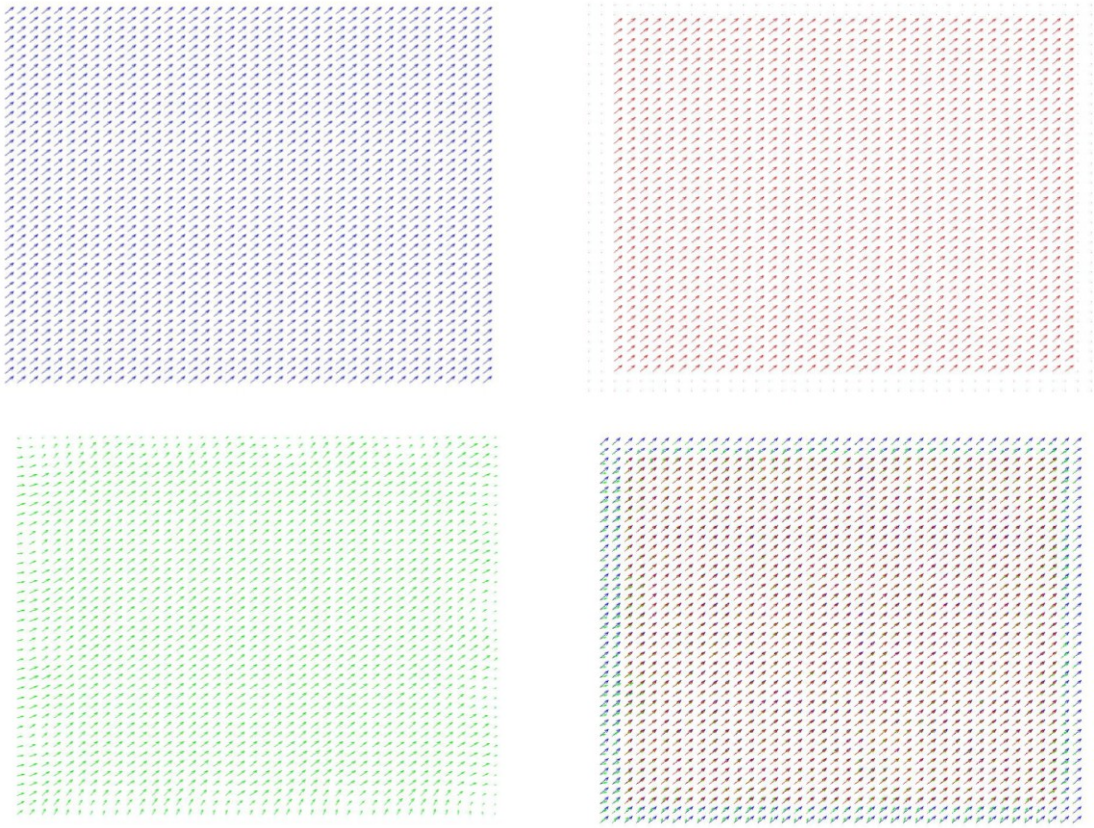

Figure 6.2: Motion Analysis Results between the Pair of Images in Figure 6.1 (from left top to right bottom):
True motion profile between the pair of images. Note that the flow vectors were scaled in length by ¾ for better visualization of the vectors;
Motion estimates from One-step algorithm;
Motion estimates from Iterative algorithm;
Display of vectors jointly by using the same color coding.

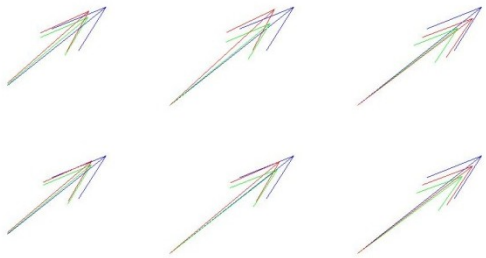

Figure 6.3: Joint Display of the Flow Vectors in Figure 6.2 Depicted in Higher Magnification. Color Code:
True Motion diagonally by 1 pixel;
Iterative OF algorithm estimated vectors;
One-step algorithm estimated vectors.

Table 6.1: Error Analysis of the Estimated Flow Vectors between the Original Noise-Free Image and its Translated Version.

Spatial Shift (diagonal)	One-step OF Algorithm		Iterative OF Algorithm	
	AE (degrees)	VLE (pixels)	AE (degrees)	VLE (pixels)
1 pixels	0.83	0.03	1.05	0.04
2 pixels	5.86	0.34	5.85	0.37
3 pixels	12.46	1.04	13.73	0.96

The error values in Table 6.1 were computed for the ideal case where the images were free of signal-independent noise. This implies that the reported values established the lower bounds for the errors to be expected when the images are corrupted by signal independent noise. Therefore, the effects of signal independent noise on the motion estimates next were investigated by changing the noise constant α

(Eq. 4.1) at increments of 0.05 for only two cases of spatial shifts by 1 and 2 pixels. The joint display of the true motion profile by 2 pixels diagonally and the estimates by both OF algorithms, as well as a magnified version of a part of the joint display, are given in Figure 6.4. The effects of the translation by 3 pixels were not studied because the errors for noise-free images for this case were already high. The results of error analysis for the estimated flow vectors from the images with the spatial shifts of 1 and 2 pixels diagonally are given in Table 6.2 and Table 6.3, respectively. As expected, the readings in the tables indicate that both estimators perform worse with increased noise. Furthermore, the closeness of the values for each noise level suggests that both estimators perform nearly equally under similar conditions of noise level and spatial shifts.

To visually compare the estimates obtained when the images were noisy, the true motion and flow estimates were simultaneously plotted in Figure 6.3. For noise-free images, the estimated vectors had good alignment with the true motion vectors in Figure 6.2, but the presence of noise in images degraded this alignment, and the degradation was greater when the noise level and spatial shift increased. These behaviors are typical and are reported to be the case for the classical motion estimators [25].

Table 6.2: Error Analysis of the Estimated Flow Vectors from Noisy Images in Case of Diagonal Translation by 1 Pixel.

Noise Constant A	One-step OF Algorithm		Iterative OF Algorithm	
	AE (degrees)	VLE (pixels)	AE (degrees)	VLE (pixels)
0.05	1.09	0.05	1.28	0.06
0.10	2.03	0.09	2.09	0.09
0.15	3.28	0.12	3.57	0.12
0.20	4.30	0.17	4.62	0.18

Table 6.3: Error Analysis of the Estimated Flow Vectors from Noisy Images in Case of Diagonal Translation by 2 Pixels.

Noise Constant A	One-step OF Algorithm		Iterative OF Algorithm	
	AE (degrees)	VLE (pixels)	AE (degrees)	VLE (pixels)
0.05	4.64	0.28	5.24	0.32
0.10	4.90	0.37	5.49	0.39
0.15	5.22	0.38	6.12	0.41
0.20	5.69	0.46	6.07	0.48

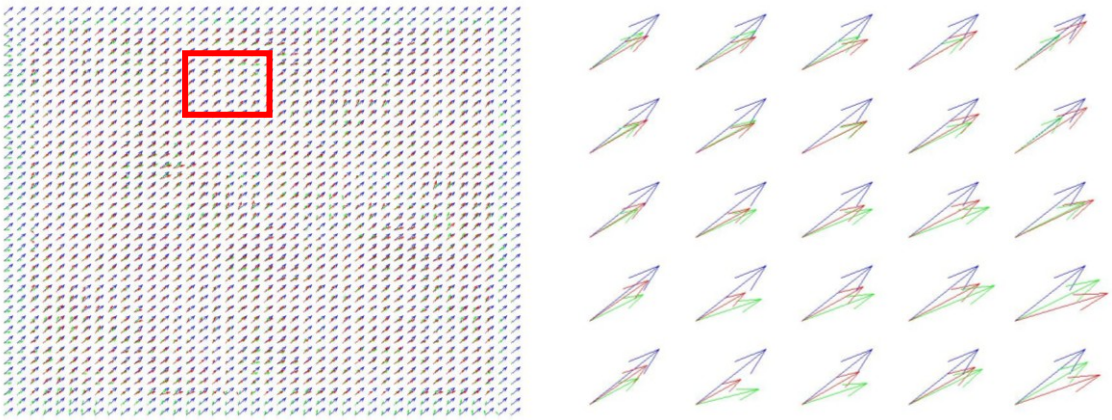

Figure 6.4: Joint Display (left) of Motion Analysis Results between the Pair of Translated Diagonally by 2 Pixels Images and its Magnified Version (right). The noise constant α = 0.2. A magnified view of the vectors from within the rectangular window is marked by the red rectangle on the left image. Color Code: → True Motion diagonally by 2 pixel; → Iterative OF algorithm estimated vectors; → One-step algorithm estimated vectors.

6.2 Inclusion with Cylindrical Geometry

The next stage of simulation experiments was carried out with a more complicated model of a hard inclusion embedded in a softer host in an environment that can best be described using cylindrical geometry. In particular, we produced square-sized synthetic tagged images of 128 pixels x 128 pixels with tag lines applied in both horizontal and vertical directions with tag spacing of 16 pixels. A cylindrical inclusion of a 25 pixel radius was centered symmetrically and assumed to be four times stiffer than the host media in order to produce a spatially varying motion profile in 2-D. The MRI pattern from this inhomogeneous simulation sample was made with slight intensity variation between the inclusion and the background. The motion experienced by the constituents of the sample under these conditions was calculated using Eq. 4.3 and Eq. 4.4. The force T applied on the compression plate was set to

0.05 kP. Vertical deformation was applied to the noise-free image using the computed motion profile. Tagged images obtained before and after the compression are shown in Figure 6.5. The true motion profile that was computed from the analytical expressions and the estimates from One-step and Iterative OF algorithms are depicted in Figure 6.6. The orientation and size variations of the vectors indicate that material in stiff inclusion experiences less motion than that of the soft background. The motion profiles along the vertical and horizontal lines crossing the center of the inclusion are plotted in Figure 6.7. Motion estimation errors were computed over a square section centered from pixels 5 to 123 in both directions, and results are found in Table 6.4 when noisy and noise-free images were considered. Unlike the case of simple translational motion studied above, the cylindrical simulation did not reveal a clear indication of an increasing trend in errors for the angle and length between the true and estimated flow vectors when noise content of the images was increased. This was an interesting finding, and instead of characterizing these errors globally over the whole image, local analysis of errors in the inclusion or identified regions in the host may be needed.

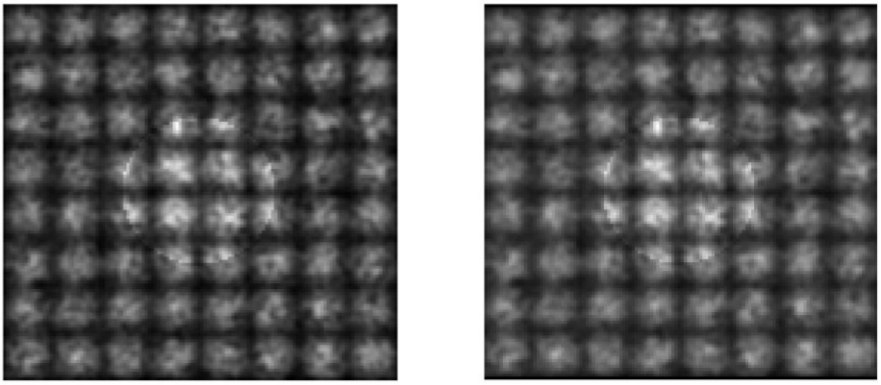

Figure 6.5: Original Noise-Free Tagged Image of the Media with the Stiff 2-D Cylindrical Inclusion (left) and its Uniformly Compressed Version (right). Uniform Compression was performed according to the analytical formulas in Eq. 4.3 and Eq. 4.4.

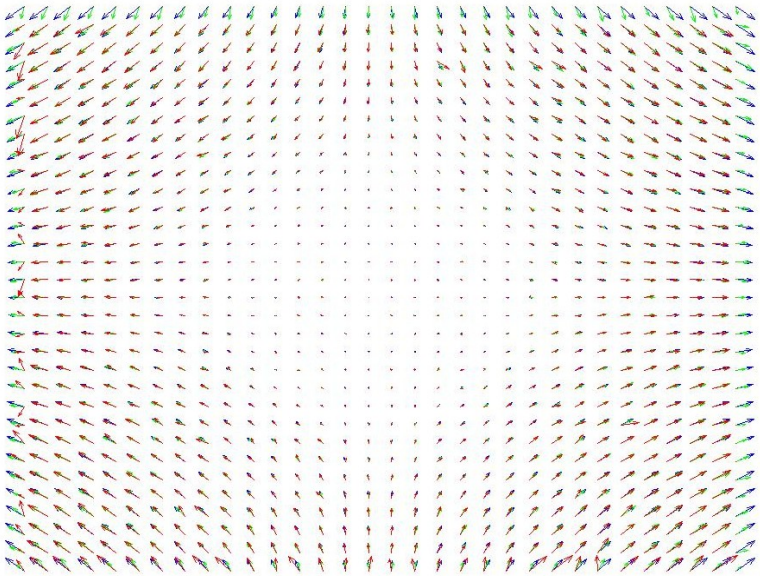

Figure 6.6: Joint Display of Motion Analysis Results between the Original and Uniformly Compressed Images with the Stiff 2-D Cylindrical Inclusion. The noise constant $\alpha = 0.05$. Color Code: → True Motion; → Iterative OF algorithm estimated vectors; → One-step algorithm estimated vectors.

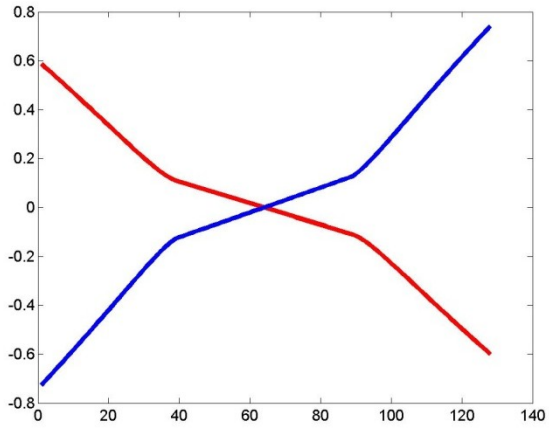

Figure 6.7: Displacement of the Material in the Sample along the Vertical (red) and the Horizontal (blue) Line Crossing at the Center of the Stiff 2-D Cylindrical Inclusion.

Table 6.4: Error Analysis of the Estimated Flow Vectors from Noisy Images with the Stiff 2-D Cylindrical Inclusion in Case of Uniform Compression.

Noise Constant	One-step OF Algorithm		Iterative OF Algorithm	
α	AE (degrees)	VLE (pixels)	AE (degrees)	VLE (pixels)
0.0	9.22	0.05	6.27	0.03
0.05	16.07	0.06	12.97	0.04
0.10	10.02	0.05	7.89	0.03
0.15	13.86	0.06	11.61	0.04
0.20	20.42	0.07	16.47	0.04

6.3 The Phantom without an Inclusion

Tagged MRI from the phantom in Figure 4.6 were acquired and processed to estimate the motion. Figure 6.8 shows the images used in the motion analysis.

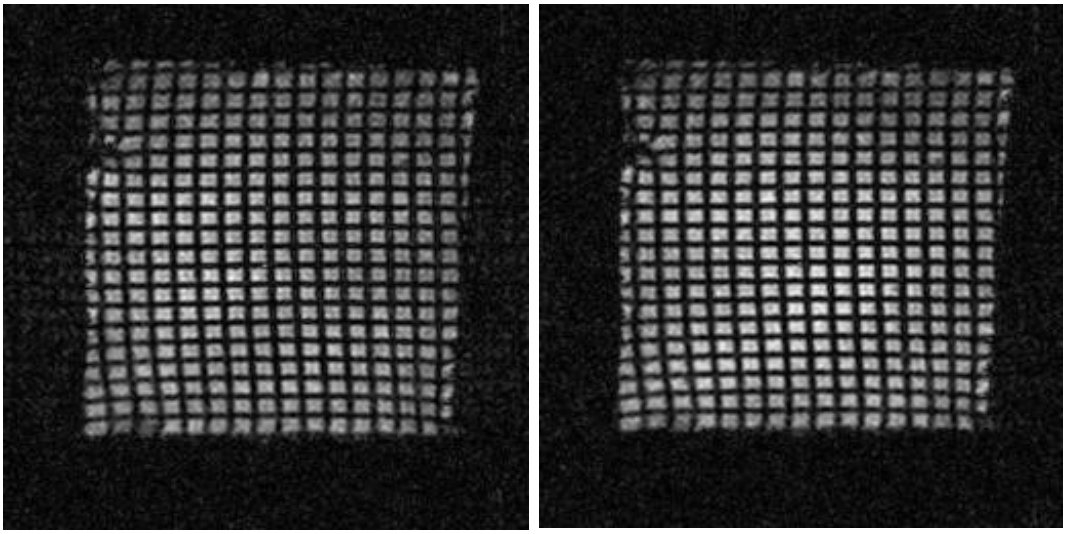

Figure 6.8: Two Consequent Images of the Compressed Agar Phantom without an Inclusion.

Both OF algorithms were tested in application to this real MRI data. The individual results for One-step and Iterative techniques are given in Figure 6.9 and 6.10 respectively. The original parameter of neighborhood window W = 5 used in the One-step algorithm in all the other studies did not produce good results. After optimization, we used W = 10, and the results improved greatly. Both original and improved estimations are provided in Figure 6.9.

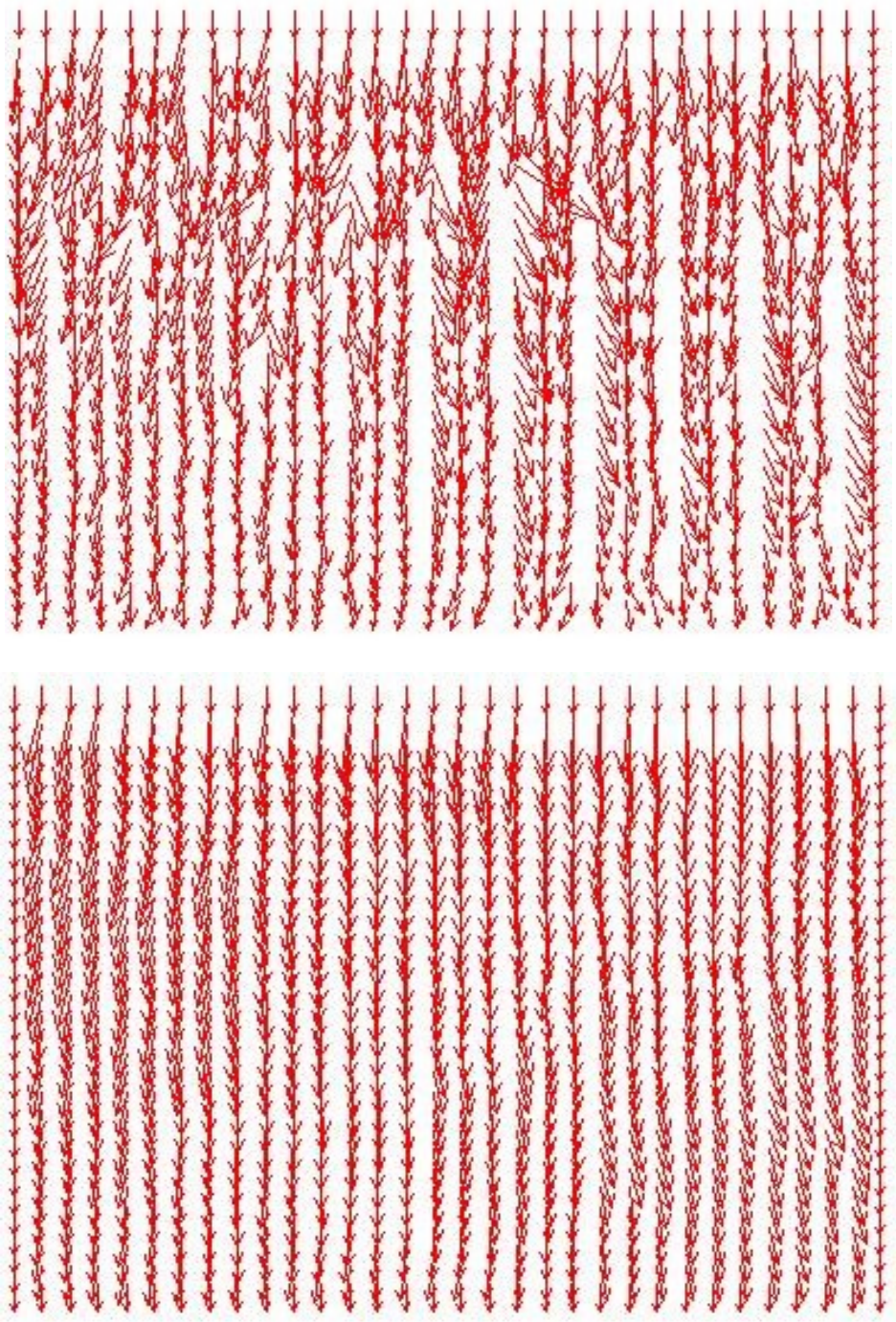

Figure 6.9: One-step OF Algorithm Motion Analysis Results between Two Consequent Images of the Compressed Agar Phantom without an Inclusion (top to bottom):
With neighborhood window W = 5;
With neighborhood window W = 10.

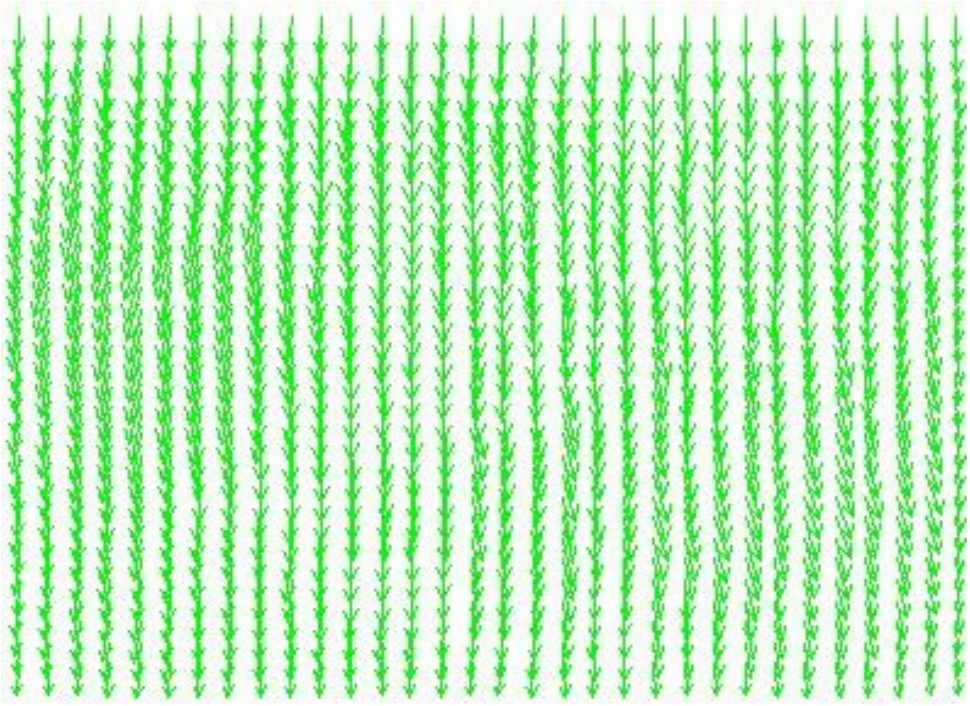

Figure 6.10: Iterative OF Algorithm Motion Analysis Results between Two Consequent Images of the Compressed Agar Phantom without an Inclusion.

Since there is no real motion profile that can be gathered for this type of data, only qualitative (visual) evaluation was possible. A joint display of the estimation results for both algorithms is given in Figure 6.11. The magnified area is marked with a red rectangle and provided in Figure 6.12.

As we can see from both Figure 6.11 and Figure 6.12, both algorithms perform well when applied to the MRI data acquired from an agar phantom with no inclusion. Also, the Iterative algorithm slightly outperformed the One-step algorithm.

There was some unusual small motion pattern present that was not expected. It is explained by either or both irregularities in the phantom texture and imperfections in

real compression introduced to the phantom during data acquisition (possible friction between the phantom and the sample holder walls), which is acceptable and frequently occurs in real data experiments. It may be possible to minimize or eliminate these irregularities by further developments and improvements of both the mechanical compression device and the agar phantom preparation and handling technologies.

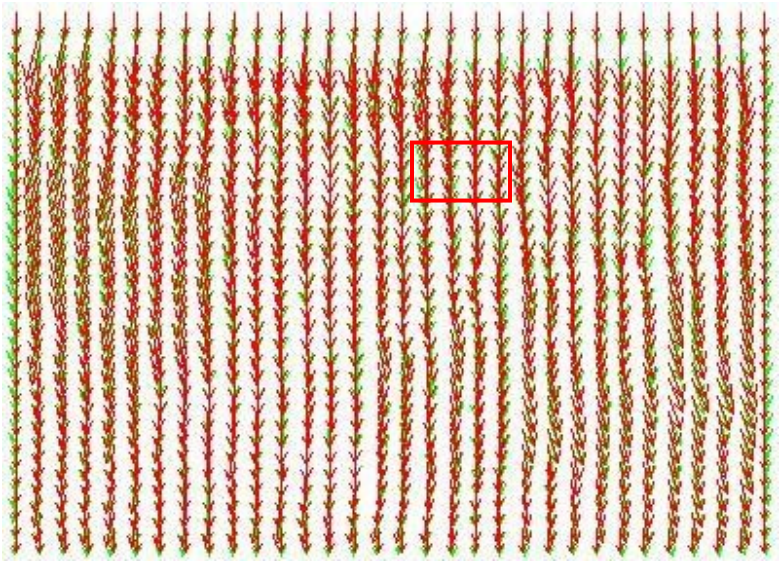

Figure 6.11: Joint Display of Motion Analysis Results between the Two Consequent Images of the Compressed Agar Phantom without an Inclusion. Color Code: → Iterative OF algorithm estimated vectors; → One-step algorithm estimated vectors.

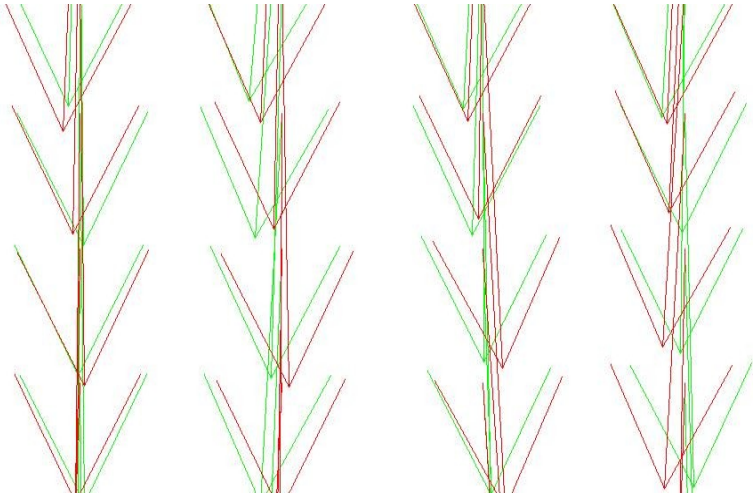

Figure 6.12: Magnified Version of the Marked by the Red Rectangle Area of Figure 6.11. Color Code: → Iterative OF, → One-step OF.

6.4 The Phantom with the Stiff Cylindrical Inclusion

Tagged MR images from the phantom in Figure 4.6 were acquired and processed to estimate the motion. Figure 6.13 shows the images used in the motion analysis.

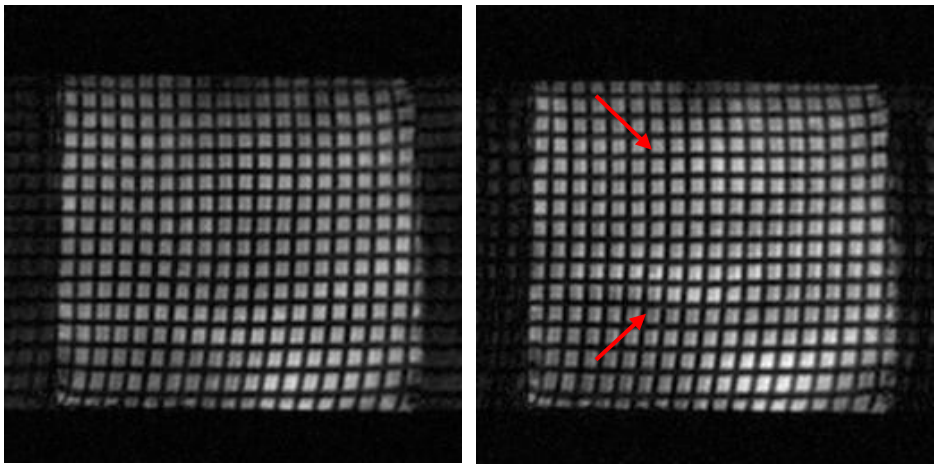

Figure 6.13: Two Consequent Images of the Compressed Agar Phantom with the Stiff Cylindrical Inclusion. The bending of the tag lines that suggests the presence of a stiff inclusion in the middle of the sample is marked by the red arrows.

By visually analyzing the MR images of the phantom presented in Figure 6.13, we can clearly see the expected bending of the tag lines in places where the inclusion and soft media strain differently with the applied compression (shown with the red arrows).

Both OF algorithms were tested in application to this phantom data. The results of One-step and Iterative algorithms are given in Figure 6.14 and Figure 6.15, respectively. In a similar manner with the estimations for the agar phantom without an inclusion, the window size in the One-step OF algorithm had to be adjusted from 5 to 10 pixels. Both estimations are provided in Figure 6.14.

Again, as in the case of the real experimental data described previously, there was no real motion profile that could be gathered for this type of data, and only a qualitative evaluation was possible to perform.

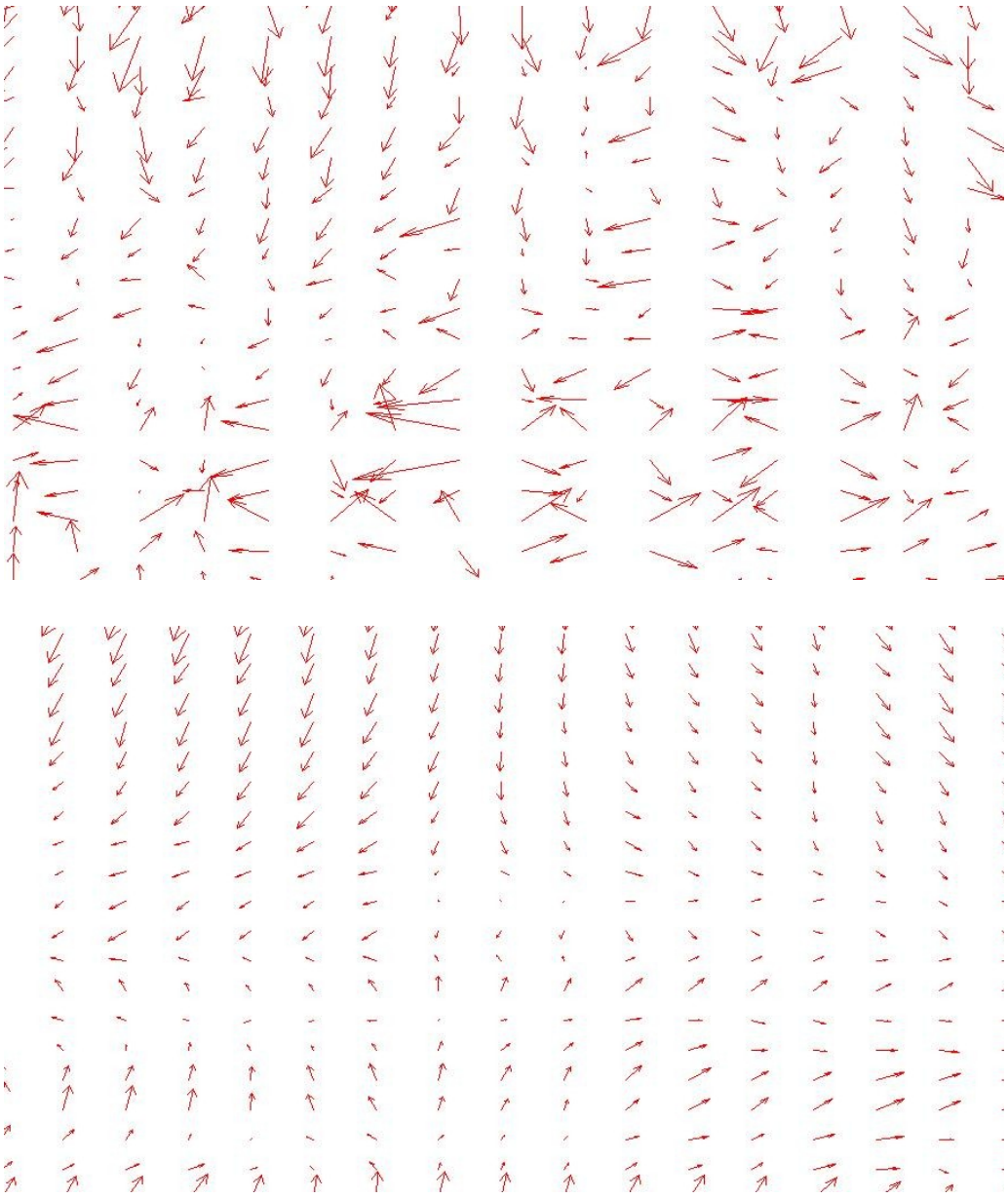

Figure 6.14: One-step OF Algorithm Motion Analysis Results between Two Consequent Images of the Compressed Agar Phantom with the Stiff Cylindrical Inclusion (top to bottom):
With neighborhood window W = 5;
With neighborhood window W = 10.

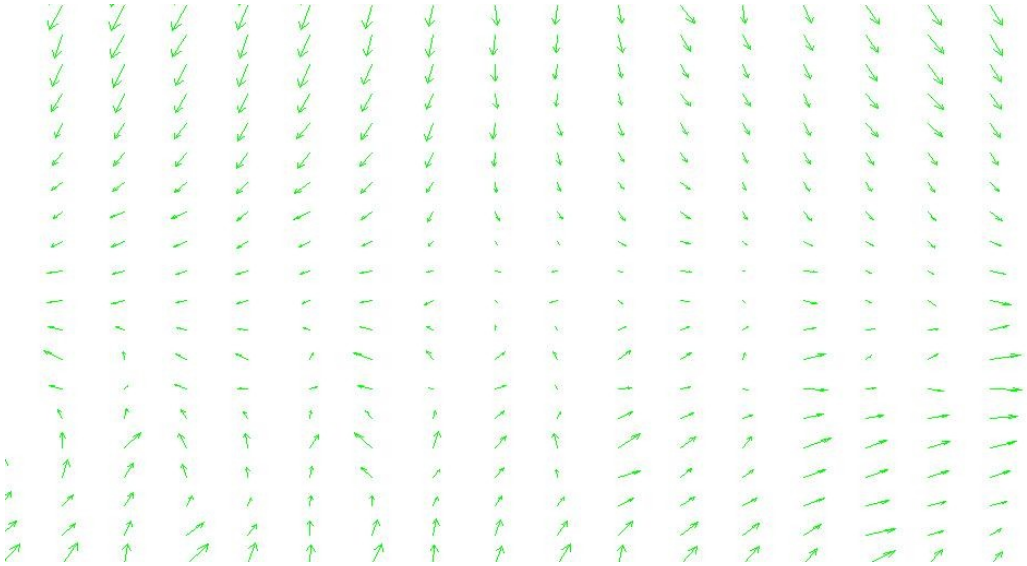

Figure 6.15: Iterative OF Algorithm Motion Analysis Results between Two Consequent Images of the Compressed Agar Phantom with the Stiff Cvlindrical Inclusion.

The joint display of estimation results by both OF algorithms is presented in Figure 6.16, and a magnified version is given in Figure 6.17. The magnified area is marked with a red rectangle in Figure 6.16.

The qualitative assessment of motion estimation by OF algorithms for this phantom showed that both techniques perform well and produce similar results after optimization of their parameters, with the Iterative technique slightly outperforming the One-step algorithm. There were some significant inconsistencies in the estimates, especially at the edges of the images. These inconsistencies, as in the case of the agar phantom without inclusion, were introduced due to the irregularities in the motion at the boundary of the phantom, such as possible friction between the phantom and the walls of the sample holder part of the compression device. This problem can be

resolved in the future by lubricating the surfaces to introduce slip boundary conditions. Overall, when the trends of the motion described by the cylindrical geometry model that was provided as a part of simulation are observed, the motion estimates suggest that there is an inclusion in the center of the sample.

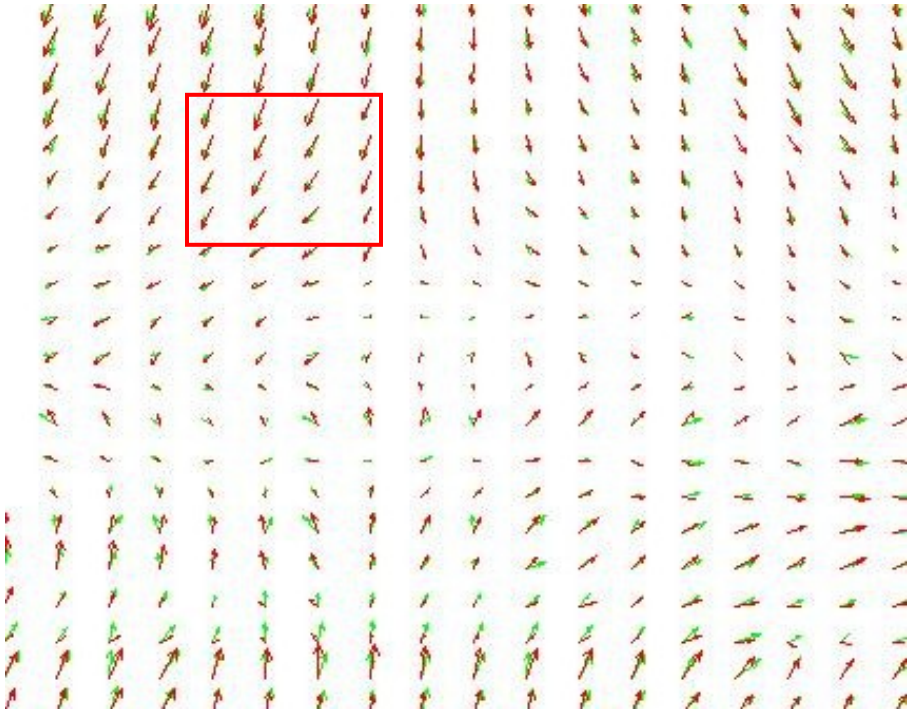

Figure 6.16: Joint Display of Motion Analysis Results between the Two Consequent Images of the Compressed Agar Phantom with the Stiff Cylindrical Inclusion. Color Code: → Iterative OF algorithm estimated vectors; → One-step algorithm estimated vectors.

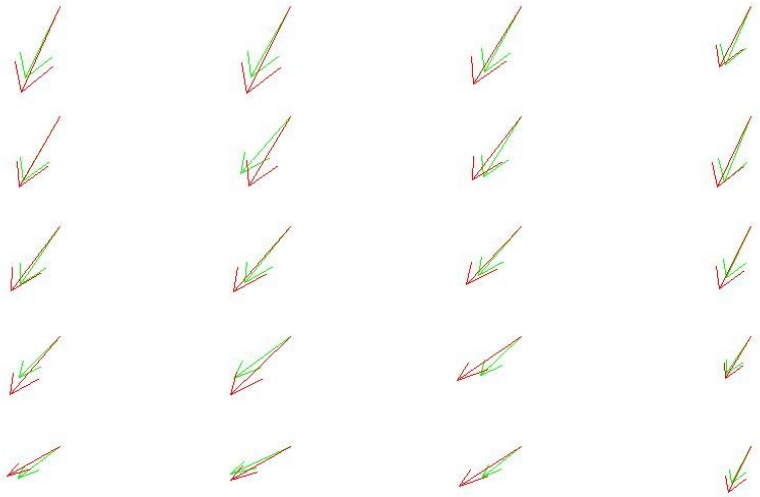

Figure 6.17: Magnified Version of the Marked by the Red Rectangle Area of Figure 6.16.

Color Code: → Iterative OF; → One-step OF.

Chapter 7.
Future Work and Other Applications

Although the results of the motion analysis from real MRE data were feasible, more studies on the phantoms with the inclusions of different bioelasticity properties are needed. Another possible extension of this research would be in application and optimization of other OF algorithms that were introduced more recently and are shown to be effective in estimating motion in a wide range of data [33, 34].

Future work includes a variety of studies on small oncology animal models followed by clinical human research [35]. While the prototype of the compression mechanism that was built as a part of our research is expected to work well in animal applications, significant adjustments should be introduced to the design of the device to use in clinical human research. Adjustments include, but are not limited to, the size of the device, its positioning/attachment to the human body, and operation with different properties of the magnetic field of the MRI scanner.

One of the other great potential areas for the development of this research is in cardio-vascular applications where regional myocardial function is assessed [36]. The motion in such applications is introduced inherently. Figure 7.1 demonstrates a series of two consequent cardiac images with tag lines similar to the ones used in MRI data acquisition.

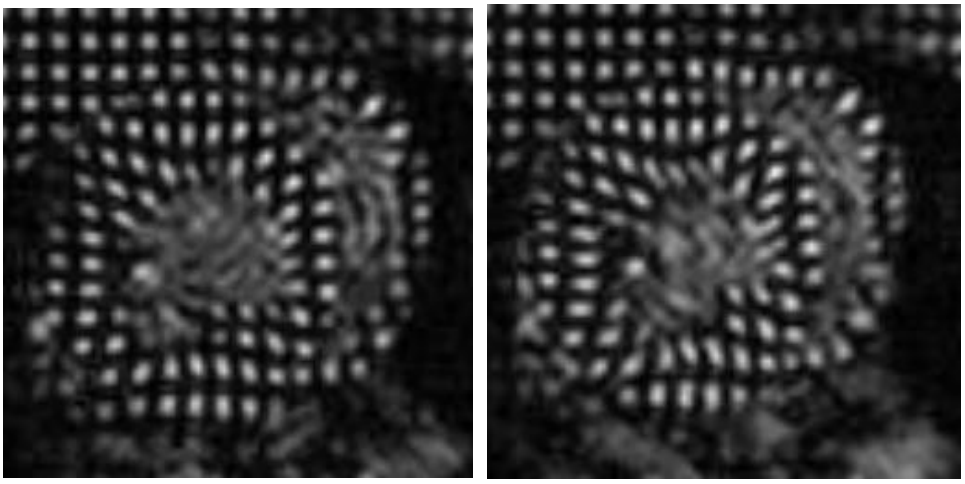

Figure 7.1: Two Consequent Cardiac Tagged Images.

The motion analysis result by the Iterative OF algorithm is presented in Figure 7.2. As we can see, flow vectors clearly depict the motion of the left ventricular wall during the cardiac cycle. The motion information can be used to estimate the regional contractility or function of the heart.

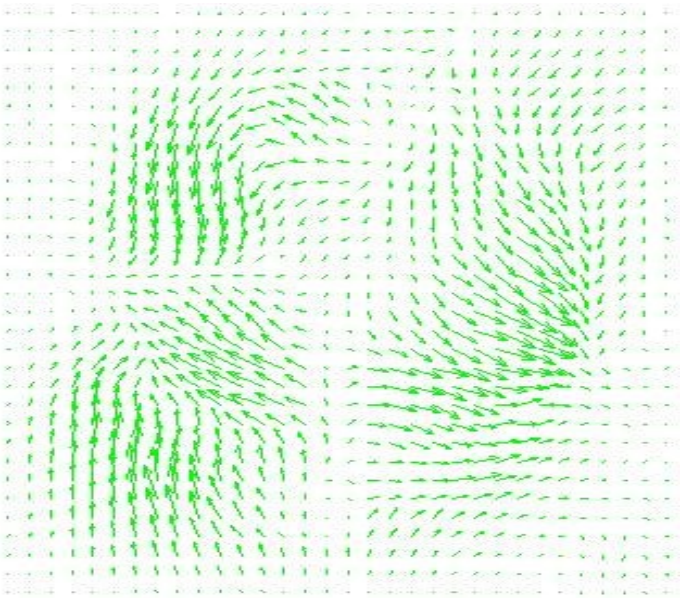

Figure 7.2: Motion Analysis Result between Two Consequent Cardiac Tagged Images.

Conclusions

Based on the results presented above, the following conclusions can be reached. The synthetic tagged images encoding either translational motion or deformation from an inclusion in cylindrical geometry were proven to be valuable numerical tools for benchmark tests. These images provided a controlled medium for testing the motion analysis algorithms, understanding the issues, determining the sensitivity of the algorithms on the noise and spatial shift, and subsequently optimizing the window size in the One-step OF algorithm or smoothness parameter in the Iterative OF algorithm. Motion analysis performed on the synthetic data using these algorithms suggested that both One-step and Iterative OF algorithms perform nearly equal when the errors in the estimates are concerned, provided that the window size or smoothness parameter is adjusted properly. In some unique cases, the Iterative OF approach may perform slightly better than the One-step approach due to the flexibility of the smoothness settings on the estimates.

The results from this research show that our optimized experimental protocols were in place to acquire reliable tagged-MRI data under the applied external compression and to estimate the resulting motion using One-step and Iterative OF algorithms. The compression instrument developed in this research was a viable tool for deforming the underlying agar-based tissue mimicking phantoms and for providing a consistent trigger signal for gating the scanner. The uniform phantoms and inhomogeneous phantoms with cylindrical inclusions remained stable and integral under the repetitive deformation applied by the compression device during

the data acquisition. The tagged MRI sequence worked well and provided quality images. However, some images suffered from susceptibility artifacts, which reflect slight perturbations in the magnetic field that commonly occur when data acquisition is carried out at high speeds. As demonstrated above, proper adjustment of the window size or smoothness parameters in the algorithms reduces the effects of these artifacts on the motion estimates.

In addition, we tested the merits of the algorithms when the tagged MRI data was acquired from myocardium undergoing an inherent contraction. The results showed that the algorithms can also be used to analyze the regional motion in the left ventricle of the heart.

Future research extends to implementations and adjustments of the mechanical compression device to perform a variety of small animal oncology studies, which would be followed by human preclinical and clinical research. The device would need to be adjusted to accommodate different size of samples and MRI scanner dimensions, as well as other parameters of data acquisitions (for example, in human research we would use a 3T MRI scanner instead of the High magnetic field MRI scanner used for our original research).

Appendix

This appendix contains Matlab software written as a part of our research. Both OF algorithms implementations as well as their testing and evaluation experiments on synthetic and phantom data are provided. The codes for the synthetic data simulations are also presented.

One-step OF Algorithm

```
function [u, v] = One_step_OF(im1, im2, windowSize);

[fx, fy, ft] = ComputeDerivatives(im1, im2);

u = zeros(size(im1));
v = zeros(size(im2));

halfWindow = floor(windowSize/2);
for i = halfWindow+1:size(fx,1)-halfWindow
   for j = halfWindow+1:size(fx,2)-halfWindow
      curFx = fx(i-halfWindow:i+halfWindow, j-
halfWindow:j+halfWindow);
      curFy = fy(i-halfWindow:i+halfWindow, j-
halfWindow:j+halfWindow);
      curFt = ft(i-halfWindow:i+halfWindow, j-
halfWindow:j+halfWindow);

      curFx = curFx';
      curFy = curFy';
      curFt = curFt';


      curFx = curFx(:);
      curFy = curFy(:);
      curFt = -curFt(:);
```

```
      A = [curFx curFy];

      U = pinv(A'*A)*A'*curFt;
      u(i,j)=U(1);
      v(i,j)=U(2);
   end;
end;

u(isnan(u))=0;
v(isnan(v))=0;


% ========== Supplementary functions
=========================
% ==== Computes horizontal, vertical and time derivatives
function [fx, fy, ft] = ComputeDerivatives(Image1,
Image2);

if (size(Image1,1) ~= size(Image2,1)) | (size(Image1,2)
~= size(Image2,2))
   error('input images are not the same size');
end;

if (size(Image1,3)~=1) | (size(Image2,3)~=1)
   error('method only works for gray-level images');
end;


fx = conv2(Image1,0.25* [-1 1; -1 1]) + conv2(Image2,
0.25*[-1 1; -1 1]);
fy = conv2(Image1, 0.25*[-1 -1; 1 1]) + conv2(Image2,
0.25*[-1 -1; 1 1]);
ft = conv2(Image1, 0.25*ones(2)) + conv2(Image2, -
0.25*ones(2));

% make same size as input
fx=fx(1:size(fx,1)-1, 1:size(fx,2)-1);
fy=fy(1:size(fy,1)-1, 1:size(fy,2)-1);
```

```
ft=ft(1:size(ft,1)-1, 1:size(ft,2)-1);
```

Iterative OF Algorithm

```
function [U,V] = Iterative_OF( Image1, Image2, niter,
lambda )
[N1,N2]=size(Image1);

PI1=zeros(N1+2,N2+2);
PI1(2:end-1,2:end-1)=Image1;
[PI11,PI12,PI13,PI14,PI15]=shifted_im(Image1);

PI2=zeros(N1+2,N2+2);
PI2(2:end-1,2:end-1)=Image2;
[PI21,PI22,PI23,PI24,PI25]=shifted_im(Image2);

Ix=border_remove(0.25*((PI13+PI23+PI15+PI25)-
(PI1+PI2+PI12+PI22)));
Iy=border_remove(0.25*((PI12+PI22+PI15+PI25)-
(PI1+PI2+PI13+PI23)));
It=border_remove(0.25*((PI2+PI22+PI23+PI25)-
(PI1+PI12+PI13+PI15)));
It=border_remove(0.25*((PI1+PI12+PI13+PI15)-
(PI2+PI22+PI23+PI25)));

Y_temp=zeros(N1,N2);
X_temp = Y_temp;

for i = 1:niter
   [Y1_temp,Y2_temp,Y3_temp,Y4_temp]=shifted_im(Y_temp);
   [X1_temp,X2_temp,X3_temp,X4_temp]=shifted_im(X_temp);

   Yk=(Y1_temp+Y2_temp+Y3_temp+Y4_temp)/4;
   Xk=(X1_temp+X2_temp+X3_temp+X4_temp)/4;
```

```
   Yn=Yk-
Ix.*(Ix.*Yk+Iy.*Xk+It).*lambda./(1+lambda*(Ix.*Ix+Iy.*Iy)
);
   Xn=Xk-
Iy.*(Ix.*Yk+Iy.*Xk+It).*lambda./(1+lambda*(Ix.*Ix+Iy.*Iy)
);

   Y_temp=Yn(2:end-1,2:end-1);
   X_temp=Xn(2:end-1,2:end-1);
end
U=X_temp;
V=Y_temp;

% ============ Supplementary functions ====================
% ==== Zeroes out the mergins of the image
function I=border_remove(I);
I(1,:)=0;
I(end,:)=0;
I(:,1)=0;
I(:,end)=0;


% ==== Shifts image over and recording modified image
matrices
function [s1,s2,s3,s4,s5]=shifted_im(Image);
[N1,N2]=size(Image);

% down
s1 = zeros(N1+2,N2+2);
s1(3:end,2:end-1)=Image;

% left
s2 = zeros(N1+2,N2+2);
s2(2:end-1,1:end-2)=Image;

% up
s3 = zeros(N1+2,N2+2);
s3(1:end-2,2:end-1)=Image;
```

```
% right
s4 = zeros(N1+2,N2+2);
s4(2:end-1,3:end)=Image;

% up-left
s5 = zeros(N1+2,N2+2);
s5(1:end-2,1:end-2)=Image;


% ==== Gaussian Smoothing
function [L,filters] = gauss_smooth(Image, sigma, shape,
radius)
nd = ndims(Image);

if(length(sigma)==1)
   sigma=repmat(sigma,[1,nd]);
end;

if(nd ~= length(sigma))
   error('Incorrect # of simgas specified');
end;

if(isa(Image, 'uint8'))
   Image = double(Image);
end;

if(nargin<3 || isempty(shape))
   shape='full';
end;

if(nargin<4 || isempty(radius))
   radius=2.25;
end;

L = Image;
filters = cell(1,nd);

for i=1:nd
   if(sigma(i)>.3)
```

```
        r = ceil(sigma(i)*radius);
        f = filter_gauss_1D(r, sigma(i));
        f = permute(f, circshift(1:nd,[1,i-1]));
        filters{i} = f;
        L = conv2(L,f,shape);
    else
        filters{i}= 1;
    end
end

% ==== Gaussian 1-D filter
function f = filter_gauss_1D(r, sigma)
if( isempty(r) )
    r = ceil(sigma*2.25);
end;

if( mod(r,1)~=0 )
    error('r must be an integer');
end;

x = -r:r;
f = exp(-(x.*x)/(2*sigma*sigma))';
f(f<eps*max(f(:))*10) = 0;
sumf = sum(f(:));

if sumf ~= 0
    f = f/sumf;
end
```

Errors Calculation

```
function [Error_Angle,Error_Length] =
errors_calculation(u,v,u_true,v_true)

size_x = size(v,1);
size_y = size(v,2);
```

```
LE = sqrt(u.^2 + v.^2);
LT = sqrt(u_true.^2 + v_true.^2);

Length_Diff= (LT-LE);
Error_Length=std2(Length_Diff);

% figure('Name','Error in Length Difference')
% imagesc(Length_Diff);
% colormap(gray)

Angle=acos( (u.*u_true+v.*v_true)./(LE.*LT)) *180/pi;  %
result is between 0 and 180


for i=1:size_x
   for j=1:size_y
      if LT(i,j)==0
         Angle(i,j)=0.0;
      end
   end
end

Error_Angle=std2(Angle);
```

Simple Translational Motion Simulation

```
close all; clear all; clc;

NY=20;
NX=20;

Y = linspace(-(NY-1),NY,2*NY);
X = linspace(-(NX-1),NX,2*NX);

im_speckle = rand(2*NY,2*NX);
im_speckle = gauss_smooth( im_speckle, 1, 'same', 5);
```

```
im_speckle = im_speckle+0.2;

w=gausswin(10,1.5);
mb=w ;
for i=1:3
   mb=[mb;w];
end
tag=mb*mb';
% to avoid 0 intensity
tag=tag+0.1;
tag_c = tag.*im_speckle;
Image1=double(tag_c);

figure('Name','Original Image')
imagesc(Image1);
colormap(gray);
axis off

% translation
dx=-2;
dy=-2;
N=20;
x = linspace(-N,N,2*N);
y = x;

[X,Y] = meshgrid(x,y);

for i=1:2*N
   for j=1:2*N
      XI_G(i,j)=X(i,j)+dx;
      YI_G(i,j)=Y(i,j)+dy;
   end
end

Imageshift = interp2(X,Y,Image1,XI_G,YI_G,'cubic');

for i=1:2*N
   for j=1:2*N
      if isnan(Imageshift(i,j))
```

```
            Imageshift(i,j) = 0;
        end
    end
end

figure('Name','Translated Tagged Image')
imagesc(Imageshift);
colormap(gray);
axis off

% imwrite(Image1,'im_0.jpg','jpg')
% imwrite(Imageshift,'im_xy.jpg','jpg')

% adding noise with same properties to both original and
translated images (separately!)
Noise_Constant = 0.2;
im_speckle_1 = rand(2*NY,2*NX);
im_speckle_1 = gauss_smooth( im_speckle_1, 1, 'same', 2);
Image1_mod = Image1 + Noise_Constant * im_speckle_1;

% figure('Name','Noise for Image 1')
% imagesc(im_speckle_1);
% colormap(gray);
% axis off
figure('Name','Original Image with Noise')
imagesc(Image1_mod);
colormap(gray);
axis off

im_speckle_2 = rand(2*NY,2*NX);
im_speckle_2 = gauss_smooth( im_speckle_2, 1, 'same', 2);
Imageshift_mod = Imageshift + Noise_Constant *
im_speckle_2;

% figure('Name','Noise for Image 2')
% imagesc(im_speckle_2);
% colormap(gray);
% axis off
```

```
figure('Name','Translated Tagged Image with Noise')
imagesc(Imageshift_mod);
colormap(gray);
axis off

% imwrite(Image1_mod,'im_0_mod.jpg','jpg')
% imwrite(Imageshift_mod,'im_xy_mod.jpg','jpg')


% true motion calculation
u_true= X-XI_G;
v_true= Y-YI_G;

figure('Name','Translated Tagged Image. True motion.
Quiver')
quiver(u_true,v_true,0.75)
colormap(gray);
axis off


% motion estimation
[U_iterative,V_iterative] = Iterative_OF(Image1_mod,
Imageshift_mod, 1000, 100);

figure('Name','Iterative OF Motion Estimation')
quiver(U_iterative,V_iterative,0.75,'g');
colormap(gray);
axis off
[U_one_step, V_one_step] = One_step_OF(Image1_mod,
Imageshift_mod, 5);
figure('Name','One-step OF Motion Estimation')
quiver(U_one_step,V_one_step,0.75,'r');
colormap(gray);
axis off

figure('Name','True Motion and Both OF Estimations')
quiver(u_true,v_true,0.75)
hold on
quiver(U_iterative,V_iterative,0.75,'g');
```

```
quiver(U_one_step,V_one_step,0.75,'r');
hold off
colormap(gray);
axis off

% segemented out internal region from (5:35,5:35) to
eliminate the edge effects
[Error_Angle_iterative,Error_Length_iterative]=
errors_calculation(U_iterative(5:35,5:35),V_iterative(5:3
5,5:35),u_true(5:35,5:35),v_true(5:35,5:35))

[Error_Angle_one_step,Error_Length_one_step]=
errors_calculation(U_one_step(5:35,5:35),V_one_step(5:35,
5:35),
u_true(5:35,5:35),v_true(5:35,5:35))
```

Cylindrical Inclusion Deformation

```
function [Image2, u_true, v_true] =
cylindrical_inclusion_deform(Image1, NY, NZ, a, T,
base_y, base_z)

% constants
mi = 4;
mm = 1;
ki = 3 - 0.45 * 4;
km = ki;

b = - 2 * (mi - mm) / (mm + mi * km);
g = (mm * (ki - 1) - mi * (km - 1)) / (2 * mi + mm * (ki
- 1));
d = (mi - mm) / (mm + mi * km);
b0 = mi * (km + 1) / (2 * mi + mm * (ki - 1));
g0 = 0;
d0 = mi * (km + 1) / (mm + mi * km);
```

```
y = linspace(-(NY - 1) * 0.1, NY * 0.1, 2 * NY);
z = linspace(-(NZ - 1) * 0.1, NZ * 0.1, 2 * NZ);

for i = 1 : 2 * NY
   for j = 1 : 2 * NZ
      radius(i,j) = sqrt(y(i)^2 + z(j)^2);
      tetaang(i,j) = atan2(y(i), z(j));
   end
end

for i = 1 : 2 * NY
   for j = 1 : 2 * NZ
      r = radius(i,j);
      teta = tetaang(i,j);

% outside of inclusion
      if r > a
         ur(i,j) = -(T / (8 * mm * r)) * ((km - 1) * r^2
+ 2 * g *a^2 + (b * (km + 1) * a^2 + 2 * r^2 + (2 * d *
(a^4) / (r^2))) * cos(2.0 * teta));
         uteta(i,j) = (T / (8 * mm * r)) * (b * (km - 1)
* a^2 + 2 * r^2 - (2 * d * (a^4) / (r^2))) * sin(2.0 *
teta);

% inside inclusion
         else
            ur(i,j) = -(T * r / (8 * mi)) * (b0 * (ki -
1) + (g0 * (ki - 3) * (r / a)^2 + 2 * d0) * cos(2 *
teta));
            uteta(i,j) = -(T * r / (8 * mi)) * (g0 * (ki
+ 3) * (r / a)^2 - 2 * d0) * sin(2.0 * teta);
         end

% True motion: conversion from cylindrical to Cartesian
geometry
% relative position to the original point
         uz(i,j) = ur(i,j) * cos(teta) - uteta(i,j) *
sin(teta);
```

```
        uy(i,j) = ur(i,j) * sin(teta) + uteta(i,j) *
cos(teta);
      end
end

% global position
yi = base_y - uy;
zi = base_z - uz;
Image2 = griddata(base_y, base_z, Image1, yi, zi,
'linear');

% motion calculation (true motion)
u_true = uz * 10;
v_true = uy * 10;
```

Tagged Images with the Stiff 2-D Cylindrical Inclusion Simulation

```
close all; clear all; clc;

NY=64;
NZ=64;
a=25;

y=linspace(-(NY-1),NY,2*NY) ;
z=linspace(-(NZ-1),NZ,2*NZ) ;

im_speckle = rand(2*NY,2*NZ);
im_speckle = gauss_smooth( im_speckle, 1, 'same', 5);

% figure('Name','Speckled Image')
% imagesc(im_speckle);
% colormap(gray);
% axis off
% imwrite(im_speckle,'im_speckle.jpg','jpg')
```

```
w=gausswin(16,1.5);
mb=w;

for i=1:7
   mb=[mb;w];
end

tag=mb*mb';
% to avoid 0 intensity
tag=tag+0.1;

% figure('Name','Tags Grid')
% imagesc(tag);
% colormap(gray);
% axis off
% imwrite(tag,'tags_grid.jpg','jpg')

tag_c = tag.*im_speckle;

% figure('Name','Tags with speckles Image')
% imagesc(tag_c_d);
% colormap(gray);
% axis off
% imwrite(tag_c_d,'tags_speckles.jpg','jpg')

for i=1:2*NY
   for j=1:2*NZ
      media(i,j) = 100;
      r=sqrt((y(i)-y(NY))^2 +(z(j)-z(NZ))^2);
      if r<a
         media(i,j) = 140;
      end
      tagged(i,j)=media(i,j) * tag_c(i,j);
      base_y(i,j)=y(i) ;
      base_z(i,j)=z(j) ;
   end
end

tagged = double(tagged);
```

```
Image1 = tagged;

figure('Name','Tagged Speckled Image with the Stiff 2-D
Cylindrical Inclusion')
imagesc(Image1);
colormap(gray);
axis off
% imwrite(Image1,'tag_speck_cylinder_incl.jpg','jpg')

T=-.05;
[Image2, u_true, v_true] =
cylindrical_inclusion_deform(Image1,NY,NZ,a,T, base_y,
base_z);
for i=1:2*NY
   for j=1:2*NZ
      if isnan(Image2(i,j))
         Image2(i,j) = 0.1;
      end
   end
end

figure('Name','Deformed Tagged Speckled Image with the
Stiff 2-D Cylindrical Inclusion')
imagesc(Image2);
colormap(gray);
axis off
colorbar
%imwrite(Image2,'tag_speck_cylinder_incl_deformed005.jpg'
,'jpg')

% adding noise with same properties to both original and
translated images (separately!)
Noise_Constant = 0.1;
im_speckle_1 = rand(2*NY,2*NZ);
im_speckle_1 = gauss_smooth( im_speckle_1, 1, 'same', 2);
Image1_mod = Image1 + Noise_Constant * im_speckle_1;

% figure('Name','Noise for Image 1')
% imagesc(im_speckle_1);
```

```
% colormap(gray);
% axis off

figure('Name','Original Image with Noise')
imagesc(Image1_mod);
colormap(gray);
axis off

im_speckle_2 = rand(2*NY,2*NZ);
im_speckle_2 = gauss_smooth( im_speckle_2, 1, 'same', 2);
Image2_mod = Image2 + Noise_Constant * im_speckle_2;
% figure('Name','Noise for Image 2')
% imagesc(im_speckle_2);
% colormap(gray);
% axis off

figure('Name','Deformed Tagged Image with Noise')
imagesc(Image2_mod);
colormap(gray);
axis off

%imwrite(Image1_mod,'tag_speck_cylinder_incl_mod.jpg','jp
g')
%imwrite(Image2_mod,'tag_speck_cylinder_incl_deformed005_
mod.jpg','jpg')

figure('Name','Deformed Tagged Image with the Stiff 2-D
Cylindrical Inclusion. True motion. Quiver')
quiver(imresize(u_true,[32 32]),imresize(v_true,[32
32]),0)
% axis off
% saveas(gcf, 'True_Motion_deformed005.jpg')

Image1_mod=Image1_mod/max(max(Image1_mod));
Image2_mod=Image2_mod/max(max(Image2_mod));

% motion estimation
[U_iterative,V_iterative] = Iterative_OF( Image1_mod,
Image2_mod, 1000, 50);
```

```
figure('Name','Iterative OF Motion Estimation')
quiver(imresize(U_iterative,[32
32]),imresize(V_iterative,[32 32]),0,'g');
colormap(gray);
% saveas(gcf, 'Iterative_cyl_incl_deformed005.jpg')

[U_one_step, V_one_step] = One_step_OF(Image1_mod,
Image2_mod, 5);
figure('Name','One-step OF Motion Estimation')
quiver(imresize(U_one_step,[32
32]),imresize(V_one_step,[32 32]),0,'r');
colormap(gray);
% saveas(gcf, 'One_step_cyl_incl.jpg')

figure('Name','True Motion and Both OF Estimations')
quiver(imresize(u_true,[32 32]),imresize(v_true,[32
32]),0)
hold on
quiver(imresize(U_iterative,[32
32]),imresize(V_iterative,[32 32]),0,'g');
quiver(imresize(U_one_step,[32
32]),imresize(V_one_step,[32 32]),0,'r');
 hold off
% saveas(gcf, 'All_OF_cyl_incl.jpg')

% segemented out internal region to eliminate the edge
effects
M1=5;M2=123;

[Error_Angle_iterative,Error_Length_iterative]=
errors_calculation(U_iterative(M1:M2,M1:M2),V_iterative(M
1:M2,M1:M2),u_true(M1:M2,M1:M2),v_true(M1:M2,M1:M2))
[Error_Angle_one_step,Error_Length_one_step]=
errors_calculation(U_one_step(M1:M2,M1:M2),V_one_step(M1:
M2,M1:M2),u_true(M1:M2,M1:M2),v_true(M1:M2,M1:M2))
```

Phantom Studies

```
close all; clear all; clc;

NY=64;
NZ=64;

% for the phantom without an inclusion
Image1=
double(imread('II_II_both_flan30_20fr_rr130.0002.jpg'));
Image2=
double(imread('II_II_both_flan30_20fr_rr130.0003.jpg'));
Image1_mod = Image1(65:192,65:192);
Image2_mod = Image2(65:192,65:192);

% for the phantom with the stiff cylindrical inclusion
% Image1 = double(imread('Im5.jpg'));
% Image2 = double(imread('Im6.jpg'));
% Image1_mod = Image1(65:192,65:192);
% Image2_mod = Image2(65:192,65:192);

% for the heart images
% Image1_mod= imresize(double(imread('heart_1.jpg')),[128
128]);
% Image2_mod= imresize(double(imread('heart_2.jpg')),[128
128]);

Image1_mod=Image1_mod/max(max(Image1_mod));
Image2_mod=Image2_mod/max(max(Image2_mod));

% motion estimation
[U_iterative,V_iterative] = Iterative_OF(Image1_mod,
Image2_mod, 1000, 1);
figure('Name','Iterative OF Motion Estimation')
quiver(imresize(U_iterative,[32
32]),imresize(V_iterative,[32 32]),0,'g');
colormap(gray);
% saveas(gcf, 'Iterative_no_incl.jpg')
```

```
[U_one_step, V_one_step] = One_step_OF(Image1_mod,
Image2_mod, 5);
figure('Name','One-step OF Motion Estimation')
quiver(imresize(U_one_step,[32
32]),imresize(V_one_step,[32 32]),0,'r');
colormap(gray);
% saveas(gcf, 'One_step_no_incl.jpg')


figure('Name','Motion Estimation')
quiver(imresize(U_iterative,[32
32]),imresize(V_iterative,[32 32]),0,'g');
hold on
quiver(imresize(U_one_step,[32
32]),imresize(V_one_step,[32 32]),0,'r');
hold off
```

References

[1] E. Haacke, *Magnetic Resonance Imaging : Physical Principles and Sequence Design*. New York: Wiley, 1999.

[2] C. Kittel, *Quantum theory of solids*. New York,: Wiley, 1963.

[3] C. Kittel, *Elementary statistical physics*. New York,: Wiley, 1958.

[4] W. Hendee, *Medical Imaging Physics*. New York: Wiley, 2002.

[5] J. Hornak, *The Basics of MRI*, 1996.

[6] C. Guy and D. Ffytche, *An Introduction to the Principles of Medical Imaging*. London: Imperial College Press, 2005.

[7] M. Bernstein, K. King, and X. Zhou, *Handbook of MRI Pulse Sequences*. Burlington: Elsevier, 2004.

[8] J. Ophir, I. Cespedes, H. Ponnekanti, Y. Yazdi, and X. Li. Elastography: a quantitative method for imaging the elasticity of biological tissues. *Ultrason Imaging.* 13: 111-34, Apr 1991.

[9] W. A. D. Anderson, *Pathology*, 1953.

[10] Y. C. Fung, *Biomechanics*. New York: Springer-Verlag, 1994.

[11] A. P. Sarvazyan. Biophysical bases of elasticity imaging. *Accoust. Imag.* 21: 223-240, 1995.

[12] T. A. Krouskop, T. M. Wheeler, F. Kallel, B. S. Garra, and T. Hall. Elastic moduli of breast and prostate tissues under compression. *Ultrason Imaging.* 20: 260-74, Oct 1998.

[13] H. Fukaya, J. Hildebrandt, and C. J. Martin. Stress-strain relations of tissue sheets undergoing uniform two dimensional stretch. *J Appl. Physiol.* 27: 758-762, 1969.

[14] H. Yamada, *Strength of biological materials*. Baltimore: Williams & Wilkins Co, 1970.

[15] H. Demiray. A note on the elasticity of soft biological tissues. *J Biomech.* 5: 309-311, 1972.

[16] K. Parker, L. Gao, R. Lerner, and S. Levinson. Imaging of the elastic properties of the tissue: A review. . *Ultrason. Med. Biol.* 22: 959-977, 1996.

[17] M. A. Dresner, G. H. Rose, P. J. Rossman, R. Muthupillai, A. Manduca, and R. L. Ehman. Magnetic resonance elastography of skeletal muscle. *J Magn Reson Imaging.* 13: 269-76, Feb 2001.

[18] R. Muthupillai, P. J. Rossman, D. J. Lomas, J. F. Greenleaf, S. J. Riederer, and R. L. Ehman. Magnetic resonance imaging of transverse acoustic strain waves. *Magn. Res. in Med.* 36: 266-274, 1996.

[19] R. Sinkus, J. Lorenzen, D. Schrader, M. Lorenzen, M. Dargatz, and D. Holz. High-resolution tensor MR elastography for breast tumour detection. *Phys Med Biol.* 45: 1649-64, Jun 2000.

[20] J. Bishop, A. Samani, J. Sciarretta, and D. Plews. Two-dimensional MR Elastography with linear inversion reconstruction: Methodology and noise analysis. *Phys. Med. Biol.* 45: 2000.

[21] J. Lorenzen, R. Sinkus, M. Biesterfeldt, and G. Adam. Menstrual-cycle dependence of breast parenchyma elasticity: Estimation with magnetic resonance elastography of breast tissue during the menstrual cycle. *Investigative Radiol.* 38: 236-240, 2003.

[22] J. Ophir, S. K. Alam, B. S. Garra, F. Kallel, E. E. Konofagou, T. Kroupskop, C. R. Merritt, R. Righetti, R. Souchon, S. Srinivasan, and T. Varghese. Elastography: imaging the elastic properties of soft tissue with ultrasound. *Med. Ultras.* 29: 155-171, 2002.

[23] M. Bilgen. Target detectability in acoustic elastography. *IEEE Trans Ultrason Ferroelectr Freq Control.* 46: 1128-33, 1999.

[24] M. Takahashi, Uematsu, H., Hatabu, H. MR Imaging at High Magnetic Fields. *Eur. J Radiol.* 46(1): 45-52, 2003.

[25] J. L. Barron, D. J. Fleet, and S. S. Beauchemin. Performance of optical flow trechniques. *IJCV*. 12(1): 43-77, 1994.

[26] R. C. Gonzalez, R. E. Woods, and S. L. Eddins, *Digital Image processing using MATLAB*. Upper Saddle River, N. J.: Pearson Prentice Hall, 2004.

[27] F. Kallel, M. Bertrand, and J. Ophir. Fundamental limitations on the contrast-transfer efficiency in elastography: an analytic study. *Ultrasound Med. Biol.* 22: 463-470, 1996.

[28] J. Maintz and M. Viergever. A survey of medical image registration. *Med. Im. Analysis.* 2: 1-36, 1998.

[29] K. P. Horn and B. G. Schunk. Determining optical flow. *AI.* 17: 185-204, 1981.

[30] J. L. Barron and N. A. Thacker. Tutorial: Computing 2D and 3D Optical Flow. *Imaging Schience and Biomedical Engineering Division, Medical School, University of Manchester, Stopford Building, Oxford Road, Manchester, 1*. 2005.

[31] B. Lucas, *Generalized image matching by the method of differences*. Carnegie Mellon University, 1984.

[32] B. Lucas and T. Kanade. An iterative image registration technique with an application to stereo vision. *in Proc. Int. Joint Conf. Artificial Intelligence.* 674-679, 1981.

[33] S. Baker, D. Scharstein, J. P. Lewis, S. Roth, M. J. Black, and R. Szeliski. A database and evaluation methodology for optical flow. *In Proc. Eleventh IEEE ICCV*. 1-8, 2007.

[34] S. Seitz, B. Curless, J. Diebel, D. Scharstein, and R. Szeliski. A comparison and evaluation of multi-view stereo reconstruction algorithms. *In Proc. CVPR.* 519-526, 2006.

[35] M. Bilgen, S. Srinivasan, L. B. Lachman, and J. Ophir. Elastography imaging of small animal oncology models: a feasibility study. *Ultrasound Med Biol.* 29: 1291-6, Sep 2003.

[36] R. Loganathan, M. Bilgen, B. Al-Hafez, M. D. Alenezy, and I. V. Smirnova. Cardiac disfunction in the diabetic rat: quantitative evaluation using high resolution magnetic resonance imaging. *Cardiovasc. Diabetol.* 5: 7, 2006.